https://doi.org/10.5194/se-2020-117
Preprint. Discussion started: 28 July 2020

Solid Earth Discussions

Coseismic fluid–rock interactions in the Beichuan-Yingxiu surface rupture zone of the Mw 7.9 Wenchuan earthquake and its implication for the fault zone transformation

Yangyang Wang [a]*, Xiaoqi Gao [a], Sijia Li [b], Shiyuan Wang [c], Deyang Shi [a,d], Weibing Shen [e]**

a The Key Laboratory of Crustal Dynamics, Institute of Crustal Dynamics, China Earthquake Administration, Beijing, 100085, China

b. Geological Exploration and Development Research Institute, Chuanqing Drilling Engineering Co., Ltd., CNPC, Chengdu, Sichuan, 610500, China.

c. Sichuan Earthquake Agency, Chengdu, 610041,China

d. Institute of Geophysics, China Earthquake Administration, Beijing, 100081, China

e. MLR Key Laboratory of Isotope Geology, Institute of Geology, Chinese Academy of Geological Sciences, Beijing 100037, China

* *Corresponding Author*

** *CO-corresponding Author*

E-mail: wyy871217@126.com

Phone number: +8615117973405

Present address: Key Laboratory of Crustal Dynamics, Institute of Crustal Dynamics, China Earthquake Administration, No. 1, Anningzhuang Road, Haidian District, Beijing, People's Republic of China, 100085

https://doi.org/10.5194/se-2020-117
Preprint. Discussion started: 28 July 2020

Solid Earth Discussions

Abstract

Mechanism of fluids in modifying mineralogy and geochemistry of the fault zone and the role of rock-fluid interaction in the faulting weakening is still debatable. Through analyzing mineralogical compositions, major elements as well as micro-structural characteristics of outcrop samples including wall rocks, low damage zone, high damage zone and oriented fault gouge samples from principal slip zone gouges, mineralogical and geochemical variations of the fault-rocks is observed from Shaba outcrop of Beichuan-Yingxiu surface rupture zone of the Mw 7.9 Wenchuan earthquake, China. The element enrichment/depletion pattern of fault rock shows excellent consistency with the variation pattern of minerals in terms of the notable feldspar alteration and decomposition, decarbonization, coseismic illitization, and chloritization that occurs in the fault zone. The Isocon analysis indicates that the overall mass loss amount of the Shaba fault zone is ranked as low damage zone < high damage zone < fault gouge, while the mass removal within the fault gouge causes the greatest loss amount in the centeral strong-deformation region. The mechanism of material loss and transformation in the fault zone, analyzed by comprehensive study, is found to be complicated: 1) during the coseismic period, the mechanical fracturing, the dehydration reaction and thermal pressurization are likely the main factors; 2) during the postseismic period, infiltration by the postseismic hydrothermal fluids is the key factor. Therefore, the coseismic mechanical fracturing, chemical reaction related to coseismic frictional heating, and postseismic fuild-rock interaction are important factors to change and control the material composition and the fault zone evolution.

Keywords: fault gouge; mass balance transfer; fluid–rock interactions; coseismic fault; Wenchuan earthquake; China

https://doi.org/10.5194/se-2020-117
Preprint. Discussion started: 28 July 2020

1. Introduction

During the seismic cycle, fluid action is commonly present in the fault zone, which mainly includes thermal pressurization and fuild-rock interaction. Thermal pressurization refers to the thermal pressurization effect of the fluid caused by rapid frictional heating, which substantially weakens the effective normal stress acting on the fault surface and the friction between two fault planes, which affects dynamic fault weakening and propagation of earthquake rupture (Sibson et al., 1973, 1990; Andrews, 2002; Wibberley and Shimamoto, 2003; Rice, 2006; Hayman et al., 2006; Mishima, 2009; Moore et al., 2013). Fluid-rock interaction means that the coseismic frictional heating intensifies the process of the fluid-rock interaction, changes the mineral composition, which mainly includes the mineral alteration/decomposition and dehydration (deaeration) (Forster et al., 1991; Hickman et al., 1995; Chen et al., 2007; Kaneko et al., 2017), and generates a large amount of layered silicate minerals (such as clay) with relatively low friction coefficient (Wintsch et al., 1995; Vrolijk et al., 1999; Fu et al., 2008; Lockner et al.,2011), which weakens the fault. The fluid action within the fault zone affects the earthquake nucleation, dynamic rupture propagation, and postseismic fault healing (Brace and Byerlee , 1966; Sibson, 1973; Beach, 1976; Bruhn et al., 1990; McCaig, 1988; Forster et al., 2007; Rice, 2006; Caine et al., 1996; Evens et al., 1995; Faulkner et al., 2003; Ishikawa et al., 2008; Hamada et al., 2009; Paola et al., 2011), the study of which has important significance.

The fluid action within the fault zone is macroscopically represented as the mineral transformation and the zoning of different mineral types and is microscopically manifested as the stability, the gain and loss of elements, and the variation in isotopic compositions (Beck et al., 1992; Thordsen et al., 2005; Wiersberg and Erzinger, 2007; Pili et al., 2011). Previous studies of the fluid action within the fault zone have focused on the material transformation, the element migration and

https://doi.org/10.5194/se-2020-117
Preprint. Discussion started: 28 July 2020

mainly use geochemical approaches to trace the sources of fluids and analyze the infiltration and fluid-rock interaction processes of fluids (Anderson et al., 1983; Evans et al., 1995; Goddard and Evans, 1995; Roland et al., 1996; Chen et al., 2007; Pili et al., 2002, 2011; Ishikawa et al., 2008; Chen et al., 2013b; Duan et al., 2016; Kaneko et al., 2017). The geochemical characteristics of fault zones cutting clastic sedimentary rocks differ from those cutting carbonate and magmatic rocks. However, the coseismic presence of fluids within the fualt zones cutting clastic sedimentary rocks and the role of fluid–rock interaction on the fault zone transformation still remain debates.

The 2008 Wenchuan Earthquake (Mw 7.9), which occurred in the Longmen Shan Fault System (LFS) on the east margin of Qinghai-Tibet Plateau, China, had never occurred since the beginning of the recorded history of the world and provides a natural experimental site for studying the fluid action with the clastic sedimentary fault zone (Ran et al., 2013; Yang et al., 2012, 2013, 2014; Yao et al., 2013; Zhang et al., 2014). The existing researches on exposures of the 2008 Wenchuan Earthquake rupture indicated that the material composition and the fault zone evolution were formed by the multistage superposition of seismic cycles (Chen et al., 2013b; Yang et al. , 2013, 2016; Duan et al., 2016). However, most relevant studies focus on the cumulative effect of long-term interseismic fluid-rock interaction, lacking of coseismic fluid-rock interaction. Besides, as the important migration pathway and activity site of fluids within the fault zone, dense fractures and secondary faults are commonly developed in the fault zones of the crust and distributed differently in various regions of the fault zone. The differential distribution of pores and cracks across the fault zone, result in various seepage channel types and fluids behaviors within different parts of the fault zone, which controls the interaction between fluids and channels and further causes the notable variation in mineral components and chemical compositions with time and space. These factors eventually affect the mechanical

https://doi.org/10.5194/se-2020-117
Preprint. Discussion started: 28 July 2020

properties and slip behaviors of faults. What are the changes in the rock mineral components and geochemical characteristics within the fault zone respond to the Wenchuan Earthquake? What is the difference of the mechanisms of material loss and transformation among the different regions across the fault zone?

Against this background, we select Shaba (SB) outcrop in the northern section of the Beichuan - Yingxiu coseismic rupture of the Wenchuan earthquake, where contains the maximum value of vertical displacement and fresh fault gouge, as the study object. This paper reports changes in the mineralogical and geochemical compositions across the fault zone through XRD、XRF and SEM-EDS at sizes of several millimeters to centimeters, attempting to analyze the mineral transformation and element migration in different regions of the fault zone at different scales during the coseismic period. In addition, this paper calculates the mass loss and element mobility within the fault zone through the Isocon, to analyse the fluid flow behavior and build material transfer patterns of fault zone cutting the clastic sedimentary rocks, in order to further study coseismic fuild-rock interaction and the role of fluid in the fault zone evolution.

2. Geological setting

The 2008 Wenchuan Earthquake, which occurred in the LFS on the east margin of Qinghai-Tibet Plateau, producing the simultaneous ruptures of two faults (Beichuan-Yingxiu surface rupture zone and Anxian-Guanxian surface rupture zone) (Xu et al., 2009; Fu et al., 2011;Yang et al. , 2014; Yao et al., 2013) (Fig.1a, b). SB outcrop in the northern section of the Beichuan - Yingxiu coseismic rupture of the Wenchuan earthquake (Fig.1b, c), where contains the maximum value of vertical displacement and fresh fault gouge. The coseismic surface rupture zone across SB area generally shows a northeastward trend, which mainly passes by the mountainside and is a continuously extending fault

https://doi.org/10.5194/se-2020-117
Preprint. Discussion started: 28 July 2020


Solid Earth
Discussions
Open Access
EGU

escarpment (Ran et al., 2008; Shi et al., 2009; Yuan et al., 2013). The original inclination of the early fracture in the fault zone in study area should be the same as the topographic slope, which are both inclined to the northwest. Due to the influence of supergene gravity, the occurrence of the fault zone in the 5-30 m segments near the ground surface is bent, reversed and countertilted to the southeast with the characteristics of normal faulting and right translation, and displacements differ at different places. In general, the vertical displacement ranges from 2.0 to 10.5 m, and the horizontal displacement ranges from 2 to 10 m. In SB area, the maximum vertical displacement ranges from 11 to 12 m; the maximum dextral horizontal displacement ranges from 12 to 15 m; and the maximum oblique slip displacement ranges from 14 to 17 m. Because the near-surface fault plane tends to reverse, this outcrop is morphologically manifested as a normal faulting strike-slip fault that tilts eastward and forms a landform of a valley within the slope (Ran et al., 2008; Yuan et al., 2013). The locations of the hanging wall and footwall of the fault are defined in terms of the surface manifestation of this fault (Ran et al., 2008; Shi et al., 2009; Yuan et al., 2013). The exploratory trench of the sampling site is perpendicular to the trending of the surface rupture zone and stretches over the hanging wall and footwall of the fault. The fault zone at the trench has a trending of NE45 °-60 ° and a dip angle of 55 °-85 °. The northwest wall is lifted, and the oblique scratches in the direction of 190 °-240 °∠40 °can be observed on the fault surface. Figure 1b shows the rupture zone of the ground surface at the trench. The footwall of the fault is the black shale of the third subgroup ($S_{2\text{-}3}$) of the Maoxian Group of the Upper and Middle Silurian, and the hanging wall is the semicemented silty clay in the Quaternary Holocene yellow slope residual diluvium (Q_{4dl+pl}). A layer of bluish gray fresh fault gouge exists between the hanging wall and the footwall of the fault, which is distributed stably and continuously and represents the coseismic fault gouge of the Wenchuan Earthquake.

https://doi.org/10.5194/se-2020-117
Preprint. Discussion started: 28 July 2020


Solid Earth Discussions

3. Field methodology and laboratory analyses

3.1 Field methodology of key outcrop and sampling procedure

Field observations show that, centered on the principal slip surface (PSS), the fault zoning in the SB outcrop is obvious and includes, from the margin to the center, wall rocks, the damage zone (including high-damaged breccia zone and low-damaged cataclasite zone), and the fault gouge (Fig. 2). The fault gouge consists of very fine, sticky particles that are easily differentiated from the surrounding rock (Fig. 2a). To obtain the geochemical and mineralogical characteristics of fault rocks in the study area, the location of the fault gouge on the PSS is placed at point zero, and the fault rock is systematically sampled across the fault zone. To ensure the accuracy of the sampling, a surface layer with a thickness of approximately 0.3 m is removed to avoid interference from weathering. Positioned according to the distance from the fault gouge, samples are collected at a maximum spacing of 3 m in the damage zone, then collected more densely towards the PSS and the sampling spacing gradually decreases to a minimum of 0.1 m approached the PSS (Fig. 2).

3.2 Chemical and mineralogical experimental method

3.2.1X-ray powder diffraction (XRD)

To identify the major and clay minerals for representative outcrop-derived samples, X-ray powder diffraction (XRD) analyses were conducted by Beijing Research Institute of Uranium Geology Analytical Laboratory. Measurements were made with a PANalytical X'Pert PRO X-ray diffractometer using Cu-Ka radiation under conditions of 40 mA and 40 kV. Diffraction patterns were obtained with 2θ range from 5° to 70° at the scanning speed of 1.0°/minute. The samples were ground below 2

https://doi.org/10.5194/se-2020-117
Preprint. Discussion started: 28 July 2020

μm grain size. The sample composition analysis is divided into two parts: rock-forming mineral analysis and clay mineral analysis. Firstly, the clay was centrifugated from the sample and the total clay content was calculated. Then non-clay minerals were directly deposited on glass slides for diffraction analysis. For analyzing the nature of clay minerals, after centrifugation, saturated glycol (EG) and high-temperature (550℃) glass slides were prepared for their XRD analyses to identify clay minerals. After diffraction analysis, each mineral contents was finally calculated. The semi-quantitative analysis of minerals is carried out on the software JADE according to the steps of background deduction, smoothing, peak search and calculation. The content of each mineral in the sample is calculated by the K value method, and the calculation formula is as follows:

$$C_i = \frac{I_i/R_i}{\sum_i^n I_i/R_i} \times 100\%$$

Where, C_i is the content of test mineral i; I_i is the diffraction intensity of the highest peak; n is the number of mineral species in the sample; R_i is the RIR value of test mineral, which is provided by the PDF card of software JADE 6.5.

3.2.2 XRF analyses

The major elements of the samples were tested by the AxiosmAX X-ray fluorescence spectrometer at the Beijing Research Institute of Uranium Geology Analytical Laboratory. Major elements of the samples were tested according to the determination of the Part 28 of chemical analysis method of silicate rocks (GB/T14506.28-2010); the ferrous oxide content were tested in accordance with Part 14 (GB/ t14506.14-2010); the LOI was tested based on rock mineral analysis (4th Ed.) Part 16.20.

https://doi.org/10.5194/se-2020-117
Preprint. Discussion started: 28 July 2020


Solid Earth Discussions

4. Results

4.1 Mineralogical results from XRD analyses

XRD mineralogical analyses were performed on the < 2 mm fraction of 15 samples across the SB outcrop corresponding to the 2008 Wenchuan earthquake, sampled from fault gouge, damaged zones and wall rocks. The major mineral assemblages and contents within the fault zone were recognized as quartz, feldspar, calcite, pyrite, gypsum and clay minerals with no detectable smectite, while pyrite and gypsum were not tested in gouge samples (Fig. 3). In general, except for individual samples ($Qtz_{SB\text{-}5\text{-}2}$%= 59.2% and $Qtz_{SB\text{-}2\text{-}6}$%= 63.5%), Qtz% of fault zone samples is relatively high and stable. Qtz% of damage zones / wall rocks samples is about 35%, while Qtz% of fault gouge samples is slightly lower, ranging from 30% to 35% basically. Potassium feldspar only exists in few samples, while plagioclase is relatively developed with range of 9.9% -33.0% in damage zones / wall rocks and less than 5% in fault gouge basically. The contents of carbonate minerals (calcite and dolomite) of fault gouge are less than those in damage zones / wall rocks. On the contrary, clay minerals were significantly developed in fault gouge, ranging from 46.2% to 62.0%, which was significantly higher than that of the surrounding damage zones / wall rocks.

Because the mineralization of the fault and the matrix cannot be completely differentiated, no significant difference between the mineral types of the wall rock and the damage zone is detected, whereas the various mineral contents of the samples from the PSS to the damage zone are notably different (Fig. 3). The mineral assemblage exhibits continuous variation from the damage zone to the fault core: (1) the content of quartz and feldspar (potassium feldspar and plagioclase) declines remarkably, and the feldspar content declines by approximately 30% and even decreases to 2.8% in

https://doi.org/10.5194/se-2020-117
Preprint. Discussion started: 28 July 2020

the fault gouge; (2) the content of carbonate minerals (calcite and dolomite) decreases and gradually becomes zero in the fault gouge (or below the detection limitation); and (3) the total amount of clay minerals increases dramatically and even increases to a maximum of 61% in the fault gouge (Fig. 3).

Note that more than 30% of the minerals in the fault zone are clay minerals, which mainly include illite, chlorite, illite/smectite mixed-layer (I/S), and a small amount of kaolinite, and the smectite exists in the form of I/S (except for sample SB-1-9, which has an S% of 2%). The content of illite and chlorite in clay minerals, which are 39%-75% and 11%-34%, respectively, are the highest, followed by the content of I/S (6%- 44%), and the I/S ratio (percentage of smectite in the I/S) almost remains between 5% and 7% (Fig. 3). A significant difference is observed between the clay minerals at various parts of the fault zone: (1) the total content of illite in the fault gouge (i.e., illite contained in I*=I/S + illite) is greater than that in the damage zone and wall rock, while the total content of smectite (S*= smectite + smectite in I/S) is smaller than that in the damage zone and wall rock; (2) the content of chlorite in the fault gouge is higher than that in the damage zone and wall rock, and the chlorite content tends to gradually increase from the high damage zone to the fault core (Fig. 3).

4.2 Elements results

The analysis of the major elements of the samples from the SB outcrop in the Beichuan-Yingxiu surface rupture zone shows that the contents of some elements are relatively stable, while the contents of other elements vary greatly, for example, Al_2O_3 (11.86%-19.21%), $Fe_2O_3^T$(3.67%-7.57%), CaO (1.19%-7.79%), Na_2O (0.554%-3.97%), and K_2O (1.54%-4.20%). Similar to the mineral composition of rocks, part of the major elements exhibit the characteristics of differential distribution in the fault zone: (1) the Al_2O_3, $Fe_2O_3^T$, and K_2O contents become increasingly towards the fault gouge and exhibit

https://doi.org/10.5194/se-2020-117
Preprint. Discussion started: 28 July 2020

significant enrichment in the fault gouge; (2) conversely, the contents of Na_2O and P_2O_5 gradually decrease towards the fault gouge and exhibit significant depletion in the fault gouge. In addition, the SiO_2 and CaO elements exhibit slight decrease towards the fault gouge, and the contents of MgO, MnO, and TiO_2 elements remain unchanged (Table1 and Fig.4).

5. Discussion

5.1 Mass balance transfer across the fault zone

The differential distribution characteristics of mineral components and elemental composition of the wall rock, damage zone, and fault gouge samples in the Beichuan-Yingxiu surface rupture zone show that coseismic fracturing, which is a nonclosed (i.e., open) dynamic geological process, is characterized by significant fuild-rock interaction, gain and loss of component/energy, and mass balance transfer across the fault zone. To eliminate to some extent the influence of the variation in the total amount of material in the nonclosed system, the element that remains relatively stable during the geological process and whose quantities (basic quantities such as mass, volume, and density) do not vary is employed as a baseline, and then the migration and variation of certain components during the geological process are quantitatively compared. According to the variation trend of chemical elements in the samples across the fault zone characterized by the bivariate diagram (Fig. 5), the Al_2O_3, $Fe_2O_3^T$, K_2O, and FeO concentrations in the fault gouge is higher than that in the damage zone, while CaO and Na_2O concentrations shows the opposite trend. The concentration of TiO_2 is relatively stable (with the maximum difference of only approximately 0.25%) and relatively high in the fault gouge, and TiO_2 has excellent correlation with other major elements (Fig. 5). Considering factors such as the activity, geological process, element content and detection limitation, the oxide of the high field-strength

https://doi.org/10.5194/se-2020-117
Preprint. Discussion started: 28 July 2020

element (HFSE) Ti is selected in this study as the immobile component, and TiO_2 wt.% is used to evaluate the relative migration rate of the rock during the alteration process in the fault zone, and the mineral alteration and dissolution-precipitation process that occur in the fault rock during the coseismic process are analyzed.

5.1.1 Mass removal in the fault gouge

Characteristics such as mineral types and contents, as well as chemical compositions of the fault gouge can be considered as the response to the mineralogical and geochemical characteristics of the fault gouge to the slip pattern and activity of the fault. A small-scale, dense sampling is conducted in the outcropping fault gouge of SB to observe the mass removal state and geochemical transformation mechanism in different regions of the fault gouge. According to the principle of mass balance, in the open process of a geological system, the wall rock sample 'O' is transformed into sample 'A' after a series of component migrations. The mass (M_k^A) of any component k in sample 'A' shall be equal to the sum of the mass (M_k^O) and transfer mass (ΔM_k^{O-A}) of the component k in sample 'O', namely:

$$M_k^A = \Delta M_k^{O-A} + M_k^O \quad (1)$$

Dividing throughout by M^O to obtain:

$$\frac{M_k^A}{M^O} = \frac{\Delta M_k^{O-A}}{M^O} + \frac{M_k^O}{M^O} = \Delta C_k^{O-A} + C_k^O \quad (2)$$

Otherwise, $C_k^A = \frac{M_k^A}{M^A} = \frac{M_k^A}{M^A}\frac{M^O}{M^O} = \frac{M^O M_k^A}{M^A M^O} = \frac{M^O}{M^A}\left(\frac{\Delta M_k^{O-A}}{M^O} + \frac{M_k^O}{M^O}\right) = \frac{M^O}{M^A}\left(\Delta C_k^{O-A} + C_k^O\right)$ (3) (Grant, 1986)

In the open process of the geological system, component Ti is selected as the immobile component, that is, there is no increase or decrease in the mass of Ti in this process, which means $\Delta C_{Ti}^{O-A} = 0$, from equation (3) we have:

$$C_{Ti}^A = \frac{M^O}{M^A} C_{Ti}^o \quad (4)$$

Therefore, this line, for which slope is equal to $\frac{M^O}{M^A}$, can be called an 'isocon', that is, a line

https://doi.org/10.5194/se-2020-117
Preprint. Discussion started: 28 July 2020


Solid Earth Discussions

253 connecting points of equal geochemical concentrations. At the same time, the slope of Isocon $\frac{M^O}{M^A}$
254 actually defines the change% in the mass of the sample before and after the geological process.

255 By this method (Grant, 1986, 2005; Gresens, 1967; O'Hara and Blackburn, 1988, 1989), mass
256 loss rate (M%) and mass balance equations can be calculated/written for six sections of the fault gouge
257 on the basis of changes in element distribution. The M% for different sections of the fault gouge are
258 slightly different (<5%), and the following pattern exists: The M% reaches the maximum at the center
259 of the fault gouge and gradually decrease towards the gouge margin. According to the results from
260 previous studies of the microstructure of the fault gouge in the SB outcrop (Yuan et al., 2013), two
261 well-developed shear planes exist near the center of the fault gouge with their direction parallel to the
262 main shear direction of the fault. These belong to Y-shear, which is the principal slip surface of the
263 Wenchuan Earthquake fault. The deformation of the fault gouge in the region between two Y-shears
264 (centeral strong-deformation region) is more intense than that on the two sides, and the microstructural
265 characteristics of various typical deformations, including Riedel shears, P-foliation, P-shear, and
266 trailing structures, are developed in this region. Thus, the slip deformation is the most concentrated in
267 this part of the earthquake. The mentioned microstructure differences among different parts of the fault
268 gouge may explain the M% differential distribution across the fault gouge to some extent: the
269 coseismic rupture causes the reduction in grain size and increase in the fuild-to-rock rate, and more
270 stress concentrated in the centeral strong-deformation region, result in the strengthening of fuild-rock
271 interaction. The mass loss amounts are the largest in the central part, followed by those on the two
272 sides, and the amount of each element lost per 100 g of wall rocks is calculated (Table 2).

https://doi.org/10.5194/se-2020-117
Preprint. Discussion started: 28 July 2020

5.1.2 Mass migration of continuous multisample system in the fault zone

Overall, the components of the rock samples in different regions undergo various degrees of transfer, that is, forming a series of samples with continuous variation in multiple components along the fault zone, rather than just two distinct samples (unchanged sample and changed sample) (Mori et al., 2007; Li et al., 2007; Beinlich et al., 2010; Guo et al. , 2009, 2013). In this study, the standardized Isocon diagram method (Anormalization solution using Isocon diagram) (Guo et al., 2009) is employed to analyze a series of samples across the fault zone of the SB outcrop.

Assume that 'O', 'A', and 'B' are a series of samples formed by progressive coseismic geochemistry and geophysics alteration in the Beichuan - Yingxiu fault zone（Fig. 6）. The relationship between sample 'O', 'A' and 'B' are described as follows:

$$C_m^A = \frac{M^O}{M^A}\left(1+\Delta C_m^{O-A}/C_m^O\right) C_m^O; \quad (5)$$

$$C_m^B = \frac{M^O}{M^B}\left(1+\Delta C_m^{O-B}/C_m^O\right) C_m^O \quad (6)$$

The immobile component T_i and mobile component m in sample B were further standardized. This standardization process provided a common Isocon line of component m in each sample without changing the M%.

The calculation using the above standardized Isocon method shows notable transfer characteristics of the major elements in a series of samples formed during the earthquake process: the major elements of the low damage zone are mostly concentrated near/on the isocon line, while those of the fault gouge are mostly distributed on the two sides (Fig. 6a), which indicates the higher transfer rate of elements in the fault gouge. Specifically, CaO, Na_2O, P_2O_5, SiO_2, LOI, and MnO are depleted in the fault core. The transfer rates of CaO and Na_2O in the fault gouge samples are the largest, with the average values of -82% and -89%, respectively (Fig. 6a). Conversely, FeO and K_2O are

https://doi.org/10.5194/se-2020-117
Preprint. Discussion started: 28 July 2020

295 significantly enriched in the fault core, with the average values of 42% and 71%, respectively, and
296 Al_2O_3 and $Fe_2O_3^T$ are slightly enriched.

297 According to the material balance equation and element transfer parameters, the fault gouge, high
298 damage zone, and low damage zone relative to the wall rock in the SB outcrop, the M% is mainly
299 ranked as low damage zone < high damage zone < fault gouge. The M% is relatively small in the low
300 damage zone, which indicates that the low damage zone mainly undergoes relatively small mechanical
301 fracturing and chemical alteration. In contrast, the M% in the high damage zone and fault gouge
302 gradually increase (Fig. 6a and Table 3), which indicates the loss of a relatively substantial amount of
303 material.

304 **5.2 Mineral and geochemical transformation during the seismic cycle**

305 **5.2.1 Decomposition and alteration of feldspar and depletion of Na and Si**

306 Towards the PSS of the study area, the feldspar content significantly decreases, while the total
307 clay content gradually increases (Fig. 3), which indicates that the dissolution and alteration of feldspar
308 minerals might occur in the fault core. The contents of Na_2O are positively correlated with the contents
309 of feldspar minerals (Fig. 7a), which means the feldspar-related alkaline earth elements (e.g., Na_2O)
310 after feldspar dissolution were taken away by fluids, which causes the notable depletion of Na_2O in
311 the fault gouge (Fig. 7a), with transfer rate of -89%, which also confirms the presence of feldspar
312 decomposition and alteration. In addition, the microscopic mineral identification shows that the
313 plagioclase in the fault gouge has apparently been altered to clay minerals (Fig. 9). Based on this
314 analysis, the formation of some neogenic clay minerals in the fault zone is related to the alteration of
315 feldspar, and the fluid-rock reaction may mainly include the alteration and transitions of plagioclase

https://doi.org/10.5194/se-2020-117
Preprint. Discussion started: 28 July 2020

316 to kaolinite and chlorite:

317 1) $2NaAlSi_3O_8$ (plagioclase) + $9H_2O+2H^+ \rightarrow Al_2Si_2O_5(OH)_4$ (kaolinite)+$2Na^+$+$4H_4SiO_4$

318 2) $2NaAlSi_3O_8$ (plagioclase) +$4(Fe, Mg)^{2+}$ +$2(Fe, Al)^{3+}$ + $10H_2O \rightarrow (Mg, Fe)_4(Fe, Al)_2Si_2O_{10}(OH)_8$

319 （chlorite） + $4SiO_2$+$2Na^+$+$12H^+$

320 These reactions generate a large amount of SiO_2 component (Goddard and Evans, 1995; Arancibia
321 et al. 2014; Duan et al., 2016), which is dissolved in the fluid (Goddard and Evans, 1995), and the
322 resulting water-soluble SiO_2 undergoes transfer and loss during the process of seismic fault slip, which
323 causes significant depletion of the SiO_2 component in the fault core.

324 **5.2.2 Transition of smectite and illite in the I/S**

325 Illite and smectite (mainly in the form of I/S) are relatively enriched within the fault zone in the
326 SB outcrop; otherwise, their contents in the wall rock and low damage zone are significantly different
327 from those in the fault gouge and high damage zone. Previous studies have shown that part of illite
328 and I/S in the fault core have been proved to be neogenic clay minerals (Solum et al., 2005; Chen et
329 al., 2007). According to the K_2O-Al_2O_3 bivariate diagram (Fig. 8a), the illitization is found to be
330 widespread within the fault zone, which provides a basis for the formation of neogenic clay minerals.
331 The degree of illitization differs at different parts of the fault zone: the degree of illitization of the fault
332 gouge is significantly higher than that of the damage zone and wall rock; and the transition rate from
333 I/S to I is relatively high (Fig. 8b).

334 The enrichment of clay minerals and the illitization within the fault core may be controlled by the
335 frictional heating, which intensifies the process of fuild-rock interaction, accelerates the alteration and
336 decomposition of minerals, and implements dehydration (deaeration). Illite and smectite are the two

https://doi.org/10.5194/se-2020-117
Preprint. Discussion started: 28 July 2020

337 2-terminal minerals of I/S. During the coseismic frictional heating, part of the interlayer water is
338 extruded from the smectite and transforms part of I/S to illite (Ma and Shimamoto, 1995; Hirose and
339 Bystricky, 2007; Sulem and Famin, 2009; Lin et al., 2013). This progressive transition from smectite
340 to illite is smectite + K^+ + Al^{3+}→1 illite + Na^+ + Ca^{2+} + Si^{4+} + Fe^{2+} + Mg^{2+} + H_2O. In this reaction
341 process, the fault can be used as a dehydration channel for the transition of I/S to illite; the fractured
342 and altered minerals (Moore et al.1997), such as feldspar provide K^+ for the formation of illite, and the
343 water-soluble SiO_2 generated from the transition may migrate and be lost along the fault (Goddard and
344 Evans, 1995; Arancibia et al. 2014; Duan et al., 2016).

345 It is worth noting that the dehydration of smectite and kaolinite can be complete during coseismic
346 period, while the transition from smectite to illite needs more time, which may explain why the
347 illitization of the smectite in the fresh coseismic fault gouge of SB is limited to the slight transition in
348 the I/S layer (transition from smectite-rich I/S to illite-rich I/S). At the same time, smectite is generally
349 formed under alkaline conditions, and the medium-acid or acidic fluid environment of SB area（Chen
350 et al., 2013b; Duan et al., 2016）may inhibits its formation.

351 **5.2.3 Decarbonization and depletion of Ca**

352 The carbonate content in the fault gouge of the SB outcrop is lower than that of the wall rock and
353 damage zone, which reflects that decarbonization may occur in the fault rock during the coseismic
354 process. Note that the presence of decarbonization of the wall rock indicates that the decarbonization
355 range is wider than the distribution range of the fault gouge. In the process of dissolution and thermal
356 decomposition of carbonate minerals, the relevant elements are prone to be removed by fluids and
357 become depleted (Chen et al., 2013b). As the main compositional element of carbonate minerals (eg.

https://doi.org/10.5194/se-2020-117
Preprint. Discussion started: 28 July 2020

358 calcite and dolomite), the contents of CaO are positively correlated with the contents of carbonate
359 minerals (Fig. 7b), which means the Ca element after feldspar dissolution were taken away by fluids,
360 the content of CaO decreases towards the fault gouge, which indicates the decarbonization, the
361 decomposition and consumption of calcite gradually strengthen towards the fault gouge (Fig. 4). In
362 addition, the microscopic mineral identification shows that the carbonate in the fault gouge has been
363 altered to clay minerals (Fig. 9); the depletion of Ca reaches the maximum in the fault gouge with the
364 highest degree of coseismic effect; and the enrichment of Ca in very few fault gouge samples is likely
365 related to the inclusion of carbonate particles and calcite-rich veins. Other major components of
366 carbonate, such as MgO and LOI, also show a similar distribution (Fig. 4).

367 **5.2.4 Extensive chloritization**

368 Compared with other outcrops of the Beichuan-Yingxiu surface rupture zone, the fault gouge at
369 the SB sampling site is rich in chlorite (with a maximum content of 25%), and the chlorite content
370 tends to gradually increase towards the fault gouge. Microscopic mineral identification shows that
371 chlorite are substantially developed in the mineral surface / gain edges and rock pores (Fig. 9), and the
372 structure of feldspar altered to chlorite often occurs in the fault gouge samples (Fig. 9), which reflects
373 the extensive chloritization in the fault zone.

374 The mineral alteration and structural characteristics of some samples of the fault gouge and
375 damage zone are observed and analyzed by combined scanning electron micrography (SEM) and
376 energy dispersive X-ray spectroscopy (EDS), which also indicates notable chloritization in the samples.
377 The figure shows the altered mineral structure at the edge of feldspar particles in the grayish green
378 fault gouge. The chlorite of altered feldspar type is distributed on the surface of feldspar, around

https://doi.org/10.5194/se-2020-117
Preprint. Discussion started: 28 July 2020

feldspar, or in cracks (Fig. 9b, c, d, e and f). The EDS analysis of feldspar particles from the middle to the edge shows that the components among feldspar particles are essentially unaffected, and the major compositional elements are Si, Al, O, and K (Fig. 10a), which suggests a typical potassium feldspar. From the middle to the edge, elements such as Fe and Mg gradually appear in the elemental composition, and the closer to the edge are the elements, the higher are the contents of the Fe and Mg elements (Fig. 10b), which are gradually consistent with the elemental composition of the surrounding neogenic clay minerals, such as chlorite. The EDS line scanning of the clay minerals formed by the alteration of feldspar particles also indicates that the newly formed minerals are characterized by progressive enrichment of Fe and Mg elements (Fig. 11).

The formation of chlorite in the fault zone occurs two ways: 1) direct decomposition of mafic silicate minerals, and 2) metasomatic alteration of Fe and Mg components caused by hydrothermal solution. Mafic minerals are not developed in the study area, which imply large amounts of chlorite are unlikely to be derived from the direct decomposition of mafic silicate minerals. Therefore, the extensive chloritization may related to the fluid environment and the ion types of fluids in the study area: the coseismic rupture causes the periodically and cyclically injected atmospheric precipitation to continuously react with the wall rock. If Mg^{2+} is added to the mentioned system, chlorite will be generated. In the study area, the feldspar alteration and decarbonization occur in the fault zone, especially the dissolution of carbonate may provide Mg^{2+} for the fluid, and the dissolution of Fe-rich dolomite could also provide Fe^{2+}. The fault zone in the study area inhibits the formation of smectite in the acidic environment and promotes the chloritization of minerals. The reaction for the chloritization and alteration of plagioclase in the fault gouge of the study area may be forms following the equation:

$$2NaAlSi_3O_8 \text{ (plagioclase)} + 4(Fe, Mg)^{2+} + 2 (Fe, Al)^{3+} + 10H_2O \rightarrow (Mg, Fe)_4(Fe,Al)_2Si_2O_{10}(OH)_8$$

https://doi.org/10.5194/se-2020-117
Preprint. Discussion started: 28 July 2020

401 $$\text{(chlorite)} + 4SiO_2 + 2Na^+ + 12H^+$$

402 **5.3 Fault zone transformation**

403 The mineral compositions and geochemical characteristics of the Beichuan-Yingxiu surface
404 rupture zone of the Wenchuan Earthquake vary with time and space, which cause a significant
405 difference in the mineral components, elemental compositions, and mass loss of rock samples among
406 different regions of the fault zone in the study area. In terms of time, the degree of the main reactions
407 (i.e., feldspar alteration, illitization, decarbonization, and chloritization) within the fault zone and the
408 mechanism of material loss and transformation are different between coseismic and postseismic
409 periods of the Wenchuan Earthquake. In terms of space, the degree of the main reactions and the
410 mechanisms of material loss and transformation are different across the fault zone including the fault
411 core and damage zone in the study area. These differences experienced temporally and spatially by the
412 fault zone affect the mechanical properties and the slip behavior of the fault.

413 In the coseismic period, the mechanical fracturing of the fault and the coseismic dehydration and
414 thermal pressurization during the coseismic friction heating are the main mechanisms that cause the
415 material loss and transformation within the fault zone. Compared with the damage zone, the fault
416 gouge of the fault core experiences stronger mechanical fracturing, coseismic dehydration, and thermal
417 pressurization, which causes greater material loss and transformation in the coseismic period but
418 relatively weaker postseismic fluid infiltration. The relatively stronger mechanical fracturing causes a
419 reduction in the grain size, which corresponds to a relatively high specific surface area and chemical
420 potential and promotes the mass loss of the fault gouge (Fig. 12). This study of Section 5.1.1. reveals
421 that the amount of mass loss reached the largest in the strong deformation region at the center of the

https://doi.org/10.5194/se-2020-117
Preprint. Discussion started: 28 July 2020

422 SB fault gouge, followed by the region on the two sides with a lesser loss, because the stress of the
423 fault gouge is more concentrated in the central region, which causes a more significant reduction in
424 grain size. The coseismic dehydration and thermal pressurization during the coseismic friction heating
425 are conducive to the accumulation of high pore pressure in the fault core, which causes material loss,
426 and the existence of notable decarbonization within the fault gouge supports this view. The coseismic
427 thermal pressurization and dehydration have an important role in promoting the fracture process,
428 especially near the surface, in the Wenchuan Earthquake. The near-surface displacement of the
429 northern segment of the fault, where the study area is located, is generally larger than the deep
430 displacement, which may be related to the abnormally high coseismic slip displacement and velocity
431 near the SB section (Chen et al., 2013b).

432 In the postseismic period, fluid infiltration is the main mechanism for material loss and
433 transformation. The postseismic fluid infiltration causes relatively stronger material loss and
434 transformation in the damage zone, while relatively weaker in the fault core. The cross-fault
435 permeability in north segment of the Beichuan-Yingxiu surface rupture zone exhibits a typical “dual
436 structure,” which is shown in other fault zones and composed of a low-permeability core, a high-
437 permeability damage zone with fracture development, and microfracture-bearing wall rock, among
438 which the fresh fault gouge has the lowest permeability (Cain, et al., 1996; Billi, 2005; Chen et al.,
439 2013b). The LOI content in the fault gouge is significantly lower than that in the damage zone in the
440 SB area (Fig. 9 and table 1), which suggests that the fault gouge has a relatively low water content and
441 its fluid permeability is lower than that of the damage zone. The “dual structure” causes the
442 interseismic fluid action in the fault zone to be mostly confined to the high-permeability damage zone.
443 Thus, the fluid can easily migrate in parallel to the fault but does not easily flow perpendicular to the

https://doi.org/10.5194/se-2020-117
Preprint. Discussion started: 28 July 2020

444 fault (Cain, et al.,1996; Billi, 2005; Chen et al., 2013b). Note that the high-porosity, high-permeability
445 damage zone with tensile fractures can provide channels for the hydrothermal fluids and promote fuild-
446 rock interaction such as mineral alteration, especially in postseismic periods when the fault valve is
447 temporarily opened. For example, typical hydrothermal minerals, such as pyrite and gypsum, are
448 developed in the damage zone in the SB area, while no minerals or veins crystallized from fluid are
449 observed in the fault gouge (Fig. 12). It indicates that the damage zone, rather than the fault gouge, is
450 the main active zone for the postseismic hydrothermal fluid. Multistage calcite veins exist in the high
451 damage zones on both sides of the fault gouge, and the fine-grained calcite veins heal the fluid channel
452 by rapid crystallization.

453 **6. Conclusions**

454 (1) The major mineral assemblages and contents within the fault zone of the SB outcrop in the
455 Beichuan-Yingxiu surface rupture zone were recognized as quartz, feldspar, calcite, pyrite, gypsum
456 and clay minerals with no detectable smectite, while pyrite and gypsum were not tested in gouge
457 samples. The mineral assemblage exhibits continuous variation from the damage zone to the fault core:
458 1) the content of quartz and feldspar (potassium feldspar and plagioclase) declines remarkably, and the
459 feldspar content declines by approximately 30% and even decreases to 2.8% in the fault gouge; 2) the
460 content of carbonate minerals (calcite and dolomite) decreases and gradually becomes zero in the fault
461 gouge (or below the detection limitation); and 3) the total amount of clay minerals increases
462 dramatically and even increases to a maximum of 61% in the fault gouge.

463 (2) The major elements of the samples from the SB outcrop in the Beichuan-Yingxiu surface
464 rupture zone shows that the contents of some elements are relatively stable, while the contents of other

https://doi.org/10.5194/se-2020-117
Preprint. Discussion started: 28 July 2020

465 elements vary greatly, such as Al_2O_3 (11.86%-19.21%), $Fe_2O_3^T$ (3.67%-7.57%), CaO (1.19%-7.79%),
466 Na_2O (0.554%-3.97%), K_2O (1.54%-4.20%). Similar to the mineral composition of rocks, part of the
467 major elements exhibit the characteristics of differential distribution in the fault zone: 1) the Al_2O_3,
468 $Fe_2O_3^T$, K_2O contents become increasingly towards the fault gouge and exhibit significant enrichment
469 in the fault gouge; 2) conversely, the contents of Na_2O and P_2O_5 gradually decrease towards the fault
470 gouge and exhibit significant depletion in the fault gouge. In addition, the SiO_2 and CaO elements
471 exhibit slight decrease towards the fault gouge, and the contents of MgO, MnO, and TiO_2 elements
472 remain unchanged.

473 (3) The Isocon analysis indicates that significant fuild-rock interaction, gain and loss of
474 component/energy, and mass balance transfer were existed across the fault zone in the study area, and
475 M% varied in different regions of the fault zone: 1) Within the fault gouge, the M% reaches the
476 maximum in the centeral strong-deformation region and gradually decrease towards the gouge margin;
477 2) Overall, the mass loss amount of the SB fault zone is ranked as low damage zone < high damage
478 zone < fault gouge.

479 (4) The notable feldspar alteration and decomposition, decarbonization, coseismic illitization, and
480 chloritization that occur in the fault zone, which generates a large amount of clay minerals and the
481 depletion of highly active elements (e.g., Na, Si, and Ca) related to feldspar and carbonate rock, as
482 well as the enrichment of elements related to aluminosilicate minerals in the core of the fault. The
483 extensive chloritization in the fault zone mainly due to metasomatic alteration of Fe and Mg
484 components caused by hydrothermal solution.

485 (5) The mechanism of material loss in the fault zone, analysed by comprehensive study, is found
486 to be complicated: 1) during the coseismic period, the mechanical fracturing, the dehydration reaction

https://doi.org/10.5194/se-2020-117
Preprint. Discussion started: 28 July 2020

and thermal pressurization caused by coseismic frictional heating are likely the main factors that result in the material loss and transformation, especially within the fault core, which is stronger than those in the damage zones; 2) during the postseismic period, it concludes that infiltration by the postseismic hydrothermal fluids mainly controlled the material loss and transformation. Due to the better permeability than the fault core, the damage zone is conducive to hydrothermal upwelling, fuild-rock interaction, and fracture healing.

Data availability

All data generated or analyzed during this study are included in this article.

Author contributions

Yangyang Wang designed and prepared the paper. Xiaoqi Gao carried out the experiment. Sijia Li, Siyuan Wang and Deyang Shi participated in the analysis and discussion of the final results. Weibing Shen supervised the preparation of the paper.

Competing interests

The authors declare that they have no conflict of interest.

Acknowledgments

This work was supported by the research grant from Institute of Crustal Dynamics, China Earthquake Administration (No. ZDJ2019-02), the special project of fundamental scientific research for the central-level public interest research institutes (No. ZDJ2017-27) from the Institute of Crustal Dynamics, China Earthquake Administration, the special project of monitoring and prediction (No.

https://doi.org/10.5194/se-2020-117
Preprint. Discussion started: 28 July 2020

506 2018020212) from China Earthquake Administration, the "insight study on the magnitude 6.6
507 earthquake in Jianghe, Xinjiang" from the Institute of Earthquake Forecasting, China Earthquake
508 Administration.

509 **References**

510 Arancibia, G., Fujita, K., Hoshino, K., et al., 2014. Hydrothermal alteration in an exhumed crustal fault
511 zone: testing geochemical mobility in the Caleta Coloso Fault, Atacama Fault System, Northern
512 Chile. Tectonophysics 623, 147–168.
513 Anderson, J.L., Osborne, R.H., Palmer, D.F., 1983. Cataclastic rocks of the San Gabriel Fault-an
514 expression of deformation at deeper crustal levels in the San Andreas fault zone. Tectonophysics
515 98, 209–251.
516 Andrews, D. J. (2002), A fault constitutive relation accounting for thermal pressurization of pore fluid.
517 J. Geophys. Res. 107, 2363.
518 Beinlich, A., Klemd, R., John, T., et al. 2010. Trace-element mobilization during Ca-metasomatism
519 along a major fluid conduit: Eclogitization of blueschist as a consequence of fluid-rock
520 interaction. Geochimica et Cosmochimica Acta, 74 (15) : 1892-1922.
521 Beck, J. R., Berndt, M. E. & Seyfried, W. E. Jr. (1992). Application of isotopic doping techniques to
522 evaluation of reaction kinetics and fluid/mineral distribution coefficients: An experimental study
523 of calcite at elevated temperatures and pressures. Chem. Geol. 97, 125–144.
524 Billi, A. (2005), Gain size distribution and thickness of breccias and gouge zones form thin (<1 m)
525 strike-slip fault cores in limestone, J. Struc. Geol., 27, 1823–1837.
526 Brace, W. F., and J. D. Byerlee (1966), Stick-slip as a mechanism for earthquakes, Science, 153, 990–

https://doi.org/10.5194/se-2020-117
Preprint. Discussion started: 28 July 2020

527 992.

528 Beach, A. (1976), The interrelations of fluid transport, deformation, geochemistry and heat flow in
529 early Proterozoic shear zones in the Lewisian Complex, Philos. Trans. R. Soc. London, Ser. A,
530 280, 569 – 604.

531 Bruhn, R.L., Yonkee, W.A., Parry, W.T., 1990. Structural and fluidchemical properties of seismogenic
532 normal faults. Tectonophysics 175, 139 – 157.

533 Caine, J. S., J. P. Evans, and C. B. Forster (1996), Fault zone architecture and permeability structure,
534 Geology, 24, 1025 – 1028.

535 Chen, W.-M. D., H. Tanaka, H.-J. Huang, C.-B. Lu, C.-Y. Lee, and C.-Y. Wang (2007), Fluid
536 infiltration associated with seismic faulting: Examining chemical and mineralogical compositions
537 of fault rocks from the active Chelungpu fault, Tectonophysics, 443, 243 – 254.

538 Chen, J.Y., Yang, X.S., Ma, S.L., Spiers, C.J., 2013b. Mass removal and clay mineral
539 dehydration/rehydration in carbonate-rich surface outcrops of the 2008 Wenchuan Earthquake
540 fault: geochemical evidence and implications for fault zone evolution and coseismic slip. J.
541 Geophys. Res. Solid Earth 118, 474 – 496.

542 De Paola, N., G. Chiodini, T. Hirose, C. Cardellini, S. Caliro, and T. Shimamoto (2011), The
543 geochemical signature caused by earthquake propagation in carbonate-hosted faults, Earth and
544 Planet. Sci. Lett., 310, 225 – 232.

545 Duan, Q.B., Yang, X.S., Ma, S.L., et al., 2016. Fluid-rock interactions in seismic faults: Implications
546 from the structures and mineralogical and geochemical compositions of drilling cores from the
547 rupture of the 2008 Wenchuan earthquake, China, Tectonophysics, 666 (2016) 260 – 280.

548 Evans, J. P., and F. M. Chester (1995), Fluid-rock interaction in faults of the San Andreas system:

https://doi.org/10.5194/se-2020-117
Preprint. Discussion started: 28 July 2020

549 Inferences from San Gabriel Fault rock geochemistry and microstructures, J. Geophys. Res., 100,
550 13,007 – 13,020, doi:10.1029/94JB02625.
551 Faulkner, D. R., A. C. Lewis and E. H. Rutter (2003), On the internal structure and mechanics of large
552 strike-slip fault zones: field observations of the Carboneras fault in southeastern Spain,
553 Tectonophysics, 367, 235 – 251.
554 Forster, C. B., and J. P. Evans (1991), Fluid flow in thrust faults and crystalline thrust sheets: Results
555 of combined field and modeling studies, Geophys. Res. Lett., 18, 979 – 982,
556 doi:10.1029/91GL00950.
557 Fu, B., Shi, P., Guo, H., Okuyama, S., Ninomiya, Y., Wright, S., 2011. Surface deformation related to
558 the 2008 Wenchuan earthquake, and mountain building of the LongmenShan, eastern Tibetan
559 Plateau. J. Asian Earth Sci. 40, 805-824.
560 Fu, B., P. Wang, P. Kong, G. Zheng, G. Wang, and P. Shi (2008), Preliminary study of coseismic fault
561 gouge occurred in the slip zone of the Wenchuan Ms 8.0 earthquake and its tectonic implications,
562 Acta Petrologica Sinica, 24(10), 2237 – 2243. (In Chinese with an English abstract)
563 Guo, S., Ye, K., Chen, Y., et al., 2009, A normalization solution to mass transfer illustration of multiple
564 progressively altered samples using the Isocon diagram, Economic Geology, v. 104, pp. 881 –
565 886.
566 Guo, S., Ye, K., Chen, Y., et al., 2013. Introduction of mass balance calculation method for component
567 transfer during the opening of a geological system. Actor Petrologica Sinica, 29 (5): 1486-1498.
568 Grant, J. A. (1986), The isocon diagram: A simple solution to Gresens' equation for metasomatic
569 alteration, Econ. Geol., 81, 1976 – 1982.
570 Grant, J. A. (2005), Isocon analysis: A brief review of the method and applications, Phys. Chem. Earth,

https://doi.org/10.5194/se-2020-117
Preprint. Discussion started: 28 July 2020

30, 997 – 1004.

Gresens, R. L. (1967), Composition-volume relationships of metasomatism, Chem. Geol., 2, 47 – 65, doi:10.1016/0009-2541(67)90004-6.

Goddard, J.V., Evans, J.P., 1995. Chemical changes and fluid–rock interaction in faults of crystalline thrust sheets, northwestern Wyoming, U.S.A. J. Struct. Geol. 17, 533–547.

Hayman, N. W., 2006, Shallow crustal fault rocks from the Black Mountain detachments, Death Valley, CA, J. Struct. Geol., 28, 1767 – 1784.

Hamada, Y., T. Hirono, W. Tanikawa, W. Soh, and S.-R. Song (2009), Energy taken up by co-seismic chemical reactions during a large earthquake: An example from the 1999 Taiwan Chi-Chi earthquake, Geophys. Res. Lett., 36, L06301, doi:10.1029/2008GL036772.

Hickman, S., R. Sibson, and R. Bruhn (1995), Introduction to special section: Mechanical involvement of fluids in faulting, J. Geophys. Res., 100(B7), 12, 831 – 840.

Hirose T, Bystricky M. 2007, Extreme dynamic weakening of faults during dehydration by coseismic shear heating. Geophys. Res. Left. 34. L14311, doi: 10.1029/2007GL030049.

Ishikawa, T., Tanimizu, M., Nagaishi, K., Matsuoka, J., Tadai, O., Sakaguchi, M., Hirono, T., Mishima, T., Tanikawa, W., Lin, W., Kikuta, H., Soh, W., Song, S.R., 2008. Coseismic fluid – rock interactions at high temperatures in the Chelungpu fault. Nat. Geosci. 1.http://dx.doi.org/10.1038/ngeo308.

Kaneko, Y., Takeshita, T., Watanabe, Y., Shigematsu, N., Fujimoto, K., 2017. Alteration reaction and mass transfer via fluids with progress of fracturing along the median tectonic line, mie prefecture, southwest Japan. In: Evolutionary Models of Convergent Margins-Origin of Their Diversity. InTechOpen, pp. 117 – 138.

https://doi.org/10.5194/se-2020-117
Preprint. Discussion started: 28 July 2020

593 Li, H.B., Wang, H., Xu, Z.Q., Si, J.L., Pei, J.L., Li, T.F., Huang, Y., Song, S.R., Kuo, L.W., Sun, Z.M.,
594 Chevalier, M.L., Liu, D.L., 2013a. Characteristics of the fault-related rocks, fault zones and the
595 principal slip zone in the Wenchuan Earthquake Fault Scientific Drilling Project Hole-1 (WFSD-
596 1). Tectonophysics 584, 23 – 42.
597 Lin A, Takano S, Hirono T, et al. 2013. Coseismic dehydration of serpentinite: Evidence from high-
598 velocity friction experiments, Chemical Geology, 344: 50-62.
599 Li, X.P., Zhang, L., Wei, C., Ai, Y., and Chen, J., 2007, Petrology of rodingite derived from eclogite in
600 western Tianshan, China: Journal of Metamorphic Geology, v. 25, p. 363 – 382.
601 Lockner, D. A., C. Morrow, D. Moore, and S. Hickman (2011), Low strength of deep San Andreas
602 Fault gouge from SAFOD core, Nature, 472, 82 – 85.
603 Ma S.L., Shimamoto Toshihiko, 1995. Effect of dehydration of montmorillonite constitutive behavior
604 of friction, Seismology and Geology, 17, 289-296.(in Chinese)
605 McCaig, A.M., 1988. Deep fluid circulation in fault zones. Geology 16, 867 – 870.
606 Mori, Y., Nishiyama, T., and Yanagi, T., 2007, Chemical mass balance in a reaction zone between
607 serpentinite and metapelites in the Nishisonogi metamorphic rocks, Kyushu, Japan: Implications
608 for devolatilization: Island Arc, v. 16, p. 28 – 39.
609 Mishima, T., Hirono, T., Nakamura, N., Tanikawa, W., Soh, W., Song, S.R., 2009. Changes to
610 magnetic minerals caused by frictional heating during the 1999 Taiwan Chi-Chi earthquake. Earth
611 Planet. Space Lett. 61, 797 – 801.
612 Moore, D.E., Lockner, D.A., 2013. Chemical controls on fault behavior: weakening of serpentinite
613 sheared against quartz-bearing rocks and its significance for fault creep in the San Andreas system.
614 J. Geophys. Res. Solid Earth 118 (5), 2558 – 2570.

https://doi.org/10.5194/se-2020-117
Preprint. Discussion started: 28 July 2020

615 Moore, D. M., and R. C. Reynolds Jr. (1997), X-Ray Diffraction and the Identification of Clay Minerals,
616 2nd ed., Oxford Univ. Press, Oxford, U. K.
617 O'Hara, K., 1988. Fluid flow and volume loss during mylonitization: an origin for phyllonite in an
618 overthrust setting, North Carolina USA. Tectonophysics 156, 21–36.
619 O'Hara, K., Blackburn, W.H., 1989. Volume-loss model for trace-element enrichments in mylonites.
620 Geology 17, 524–527.
621 Pili, E., F. Poitrasson, and J. P. Gratier (2002), Carbon-oxygen isotope and trace element constraints
622 on how fluids percolate faulted limestones from the San Andreas Fault system: partitioning of
623 fluid sources and pathways, Chem. Geol., 190, 231–250.
624 Pili, E., B. M. Kennedy, M. E. Conrad, and J.-P. Gratier (2011), Isotopic evidence for the infiltration
625 of mantle and metamorphic CO_2-H_2O fluids from below in faulted rocks from the San Andreas
626 Fault System, Chem. Geol., 281(3-4), 242–252.
627 Ran, Y.K., Chen, W.S., Xu, X.W., Chen, L.C., Wang, H., Yang, C.C., Dong, S.P., 2013. Paleoseismic
628 events and recurrence interval along the Beichuan–Yingxiu fault of Longmenshan fault zone,
629 Yingxiu, Sichuan, China. Tectonophysics 584, 81–90.
630 Ran, Y.K., Chen L.K., Chen, G.H., et al. 2008. Primary analyses of in-situ recurrence of large
631 earthquake along seismogenic fault of the Ms 8. 0 Wenchuan earthquake. Seismology and
632 Geology, 30, 630-643. (in Chinese).
633 Rice, J. R. (2006), Heating and weakening of faults during earthquake slip. J. Geophys. Res. 111,
634 B05311.
635 Roland, P., Ola, K., 1996. Physico/chemical stability of smectite clays. Eng. Geol. 41, 73–85.
636 Solum, J.G., van da Pluijm B. A., Peacor, D., 2005. Neocrystallization, fabrics and age of clay minerals

https://doi.org/10.5194/se-2020-117
Preprint. Discussion started: 28 July 2020

637 from an exposure of the Moab Fault, Utah. Journal of Structural Geology, 27, 1563-1576.
638 Solum, J.G., Famin, V., 2009. Thermal decomposition of carbonates in fault zones: Slip-weakening
639 and temperature-limiting effects. Journal of Geophysical Research: Solid Earth 114(B3),
640 http://dx.doi.org/10.1029/2008JB006004
641 Sibson, R. H. (1973), Interaction between temperature and pore-fluid pressure during earthquake
642 faulting-A mechanism for partial or total stress relief, Nature, 243, 66 – 68.
643 Sibson, R. H. (1990), Conditions for fault-valve behavior, Geol. Soc., London, Special Publications,
644 54, 15 – 28.
645 Shi, X., Ran, Y.K., Chen L.K., et al. 2009. Preliminary study on paleoearthquake at Beichuan-Dengjia
646 segment along the central fault of Longmen Mountains . Quaternary Soiences 29 (3): 494-501.
647 (in Chinese)
648 Thordsen, J. J., W. C. Evans, Y. K. Kharaka, B. M. Kennedy, and M. van Soestim (2005), Chemical
649 and isotopic composition of water and gases from the SAFOD wells: Implications to the dynamics
650 of the San Andreas Fault at Parkfield, CA, Eos Trans. AGU, 86(52), Fall Meet. Suppl., Abstract
651 T23E – 08.
652 Vrolijk, P., van der Pluijm, B.A., 1999. Clay gouge. J. Struct. Geol. 21, 1039 – 1048.
653 Wibberley, C. A. J., and T. Shimamoto (2003), Internal structure and permeability of major strike-slip
654 fault zones: the Median Tectonic Line in Mie Prefecture, Southwest Japan, J. Struct. Geol., 25,
655 59 – 78.
656 Wintsch, R.P., Christoffersen, R., Kronenberg, A.K., 1995. Fluid – rock reaction weakening of fault
657 zones. J. Geophys. Res. 100(13), 21 – 32.
658 Wiersberg, T., and J. Erzinger (2007), A helium isotope cross-section study through the San Andreas

https://doi.org/10.5194/se-2020-117
Preprint. Discussion started: 28 July 2020

659 Fault at seismogenic depths, Geochem. Geophys. Geosyst., 8(1), Q01002,
660 doi:10.1029/2006GC001388.
661 Xu, X., X. Wen, G. Yu, G. Chen, Y. Klinger, J. Hubbard, and J. Shaw (2009), Coseismic reverse- and
662 oblique-slip surface faulting generated by the 2008 Mw 7.9 Wenchuan earthquake, China,
663 Geology, 37(6), 515 – 518.
664 Yang T, Chen J, Yang X, et al. Differences in magnetic properties of fragments and matrix of breccias
665 from the rupture of the 2008 Wenchuan earthquake, China: Relationship to faulting.
666 Tectonophysics, 2013, 601(5): 112-124.
667 Yang T, X Yang, Q Duan, et al. 2016, Rock magnetic expression of fluid infiltration in the Yingxiu-
668 Beichuan fault (Longmen Shan thrust belt, China), Geochem. Geophys. Geosyst., 17, 1065-1085,
669 doi:10.1002/2015SGC006095.
670 Yang, T., Chen, J., Wang, H., Jin, H., 2012. Rock magnetic properties of fault rocks from the rupture
671 of the 2008 Wenchuan earthquake, China and their implications: preliminary results from the
672 Zhaojiagou outcrop, Beichuan County (Sichuan). Tectonophysics 530, 331–341.
673 Yang, T., Chen, J., Yang, X., Wang, H., Jin, H., 2013. Differences in magnetic properties of fragments
674 and matrix of breccias from the rupture of the 2008 Wenchuan earthquake, China: relationship to
675 faulting. Tectonophysics 601, 112–124.
676 Yang, X.S., Yang, Y., Chen, J.Y., 2014. Pressure dependence of density, porosity, compressional wave
677 velocity of fault rocks from the ruptures of the 2008 Wenchuan earthquake, China.
678 Tectonophysics 619, 133–142.
679 Yao, L., Ma, S.L., Shimamoto, T., Togo, T., 2013. Structures and high-velocity frictional properties of
680 the Pingxi fault zone in the Longmenshan fault system, Sichuan, China, activated during the 2008

https://doi.org/10.5194/se-2020-117
Preprint. Discussion started: 28 July 2020

Wenchuan earthquake. Tectonophysics 599, 135–156.

Yuan, R.M., Zhang, B.L., Xu, X.W., Lin, C.Y., 2013. The microstructures and clay mineral characteristics of fault gouge in the northern section of Beichuan - Yingxiu fault in Wenchuan earthquake and its significance, Seismology and Geology, 35, 685-699. (in Chinese).

Zhang, L., He, C.R., 2013. Frictional properties of natural gouges from Longmenshan fault zone ruptured during the Wenchuan Mw7. 9 earthquake. Tectonophysics 594, 149–164.

Table captions

Table 1. Average major element composition of the fault gouge and the rocks from the high / low damage zones and the SB outcrop.

Table 2. The material balance equation of samples within the fault gouge and the corresponding mass loss rates (%).

Table 3. The material balance equation of samples across the fault zone and the corresponding mass loss rates (%).

Figure captions

Figure 1. Maps showing the structural settings and location of the Shaba (SB) outcrop. (a) tectonic setting of the Longmen Shan Fault System (LFS). Modified from Li et al. (2013a). (b) The district-scale map showing the lithology and main branches of the Yingxiu-Beichuan fault around SB area. (c) Regional distribution of Sichuan Basin and magnitude distribution in China.

Figure 2. SB outcrop: general observation. (a) Photograph of the SB outcrop with the coseismic fault gouge and location of the sampling sites. (b) Fault gouge sampled using metal tubes (the gouge was sampled, consolidated, and then cut to prepare thin sections of gouge sample after consolidation). (c)

https://doi.org/10.5194/se-2020-117
Preprint. Discussion started: 28 July 2020

Geological map of the SB outcrop.

Figure 3. Variation in major and clay mineral contents across the SB outcrop. Different shades of yellow, from dark to light, represents the fault gouge, the high damage zone, and the low damage zone, respectively. The black dashed lines represent the varying trends.

Figure 4. Variation in major elements contents across the SB outcrop. Different shades of yellow, from dark to light, represents the fault gouge, the high damage zone, and the low damage zone, respectively. The black dashed lines represent the varying trends.

Figure 5. Major element comparisons over TiO_2 wt % to evaluate relative mobility during alteration. Circles represent samples from wall rocks and damage zones, and triangles represent fault gouge. (a) TiO_2 vs. Al_2O_3; (b) TiO_2 vs. Na_2O;(c) TiO_2 vs. Fe_2O_3; (d) TiO_2 vs. K_2O; (e) TiO_2 vs. MgO; (f) TiO_2 vs. FeO; (g) TiO_2 vs. CaO; (h) TiO_2 vs. P_2O_5; (i) TiO_2 vs. MgO; (j) TiO_2 vs. LOI.

Figure 6. (a) A normalized Isocon diagram for the SB outcrop using the normalization solution. The thick line indicates the unified isocon defined by TiO_2; the numbers before the oxide symbol represent the scaling coefficients; and (b) Schematic illustration of mass changes in a three-sample system.

F**igure 7**. (a) Na_2O concentrations vs. feldspar minerals concentrations; and (b) CaO concentrations vs. carbonate minerals concentrations of wall rock, high damage zone, low damage zone and fault gouge at the SB outcrop.

Figure 8. (a) Al_2O_3 concentrations vs. K_2O concentrations of wall rock, high damage zone, low damage zone and fault gouge at the SB outcrop. Ⅰ represents fault gouge and high damage zone samples and most of low damage zone sample underwent illitization； Ⅱ represents wall rock samples and one of low damage zone sample which did not undergo illitization. (b) illite concentrations vs. I/S layer concentrations of wall rock, high damage zone, low damage zone and fault gouge at the SB

https://doi.org/10.5194/se-2020-117
Preprint. Discussion started: 28 July 2020

724 outcrop.

725 **Figure 9.** Microphotographs of the rock units. All samples are from fault gouge. (a) carbonate minerals
726 which altered to some clay minerals. (b), (c), (d), (e) and (f) feldspar and other minerals which altered
727 to chlorite. (b), (c), (d) and (e) images are presented in plane polarized light, and (a) and (f) image is
728 present in crossed polarized light.

729 **Figure 10.** EDS point analysis of feldspar particles in the middle location and the edge location. (a)
730 and (b) are the microphotographs of the rock units and the element contents for the middle and the
731 edge point, respectively.

732 **Figure 11**. EDS line scanning of the clay minerals formed by the alteration of feldspar particles. (a)
733 microphotographs of the rock units; (b) distribution of the main element contents, (c) distribution of
734 the Fe contents, (d) distribution of the Mg contents, (e) distribution of the Si contents.

735 **Figure 12**. The conceptual model showing geochemical and geophysical processes of faults in the
736 seismic period.

https://doi.org/10.5194/se-2020-117
Preprint. Discussion started: 28 July 2020

Solid Earth Discussions

737

738 **Table 1**

Major element	Fault gouge (Five samples)	High damage zone (Four samples)	Low damaged zone (Four samples)	Wall rocks (Two samples)
SiO_2	60.07	61.23	61.08	59.77
Al_2O_3	17.45	14.33	12.99	11.87
$Fe_2O_3^T$	6.37	5.10	4.70	3.73
MgO	2.44	2.95	2.61	1.95
CaO	2.03	2.72	4.45	7.77
Na_2O	0.59	2.44	2.86	3.69
K_2O	3.90	2.84	2.22	1.59
MnO	0.08	0.05	0.08	0.11
TiO_2	0.71	0.68	0.61	0.49
P_2O_5	0.19	0.21	0.22	0.23
LOI	5.72	6.92	7.76	8.25
FeO	3.80	2.82	2.25	1.86

739 * Major element data are in wt.%. Major element contents are the average values.

https://doi.org/10.5194/se-2020-117
Preprint. Discussion started: 28 July 2020

740 **Table 2**

Sample	Material balance equation	M%
SB-1-7	100 g wall rock – 15.00 g SiO_2 – 1.61 g Al_2O_3 – 5.34 g CaO – 2.54 g Na_2O – 0.07 g MnO_2 – 3.72 g LOI – 0.07 g P_2O_5 → 72.74 g gouge + 0.02 g $Fe_2O_3^T$ + 0.53 g MgO +0.54 g K2O	27.26
SB-3-1	100 g wall rock – 17.54 g SiO_2 – 0.13 g Al_2O_3 – 4.68 g CaO – 3.53 g Na_2O – 0.03 g MnO_2 – 3.33 g LOI – 0.14 g P_2O_5 → 72.24 g gouge + 0.50 g $Fe_2O_3^T$ + 0.06 g MgO + 1.09 g K_2O	27.76
SB-1-8	100 g wall rock – 19.32 g SiO_2 – 6.94 g CaO – 3.59 g Na_2O – 0.04 g MnO_2 – 5.13 g LOI – 0.15 g P_2O_5 → 68.38 g gouge + 0.89 g $Fe_2O_3^T$ + 1.17 g Al_2O_3 + 0.19 g MgO + 1.31g K_2O	31.62
SB-1-9	100 g wall rock – 20.02 g SiO_2 – 6.92 g CaO – 3.59 g Na_2O – 0.05 g MnO_2 – 5.13 g LOI – 0.17 g P_2O_5 → 68.38 g gouge + 1.30 g $Fe_2O_3^T$ + 0.8 g Al_2O_3+ 0.19 g MgO + 1.27 g K_2O	31.67
SB-2-1	100 g wall rock – 17.08 g SiO_2 – 6.84 g CaO – 3.57 g Na_2O – 0.05 g MnO_2 – 5.13 g LOI – 0.16 g P_2O_5 → 67.31g gouge + 0.82 g $Fe_2O_3^T$ + 0.59 g Al_2O_3 + 0.19 g MgO + 1.18g K_2O	32.69
SB-4-1	100 g wall rock – 13.47 g SiO_2 – 0.11 g Al_2O_3 – 0.32 g $Fe_2O_3^T$ – 6.21 g CaO – 3.50 g Na_2O – 0.04 g MnO_2 – 5.13 g LOI →70.2 g gouge + 0.19 g MgO + 1.00 g K_2O + 0.12 g P_2O_5	29.8

741

https://doi.org/10.5194/se-2020-117
Preprint. Discussion started: 28 July 2020

742 **Table 3**

Fault zone subdivision (sample numbers)	Material balance equation	M%
Fault gouge (5)	100 g wall rock – 18.11 g SiO_2 – 0.26 g MgO – 6.36 g CaO – 3.27 g Na_2O – 0.05 g MnO_2 – 4.28 g LOI – 0.10 g P_2O_5 → 69.63 g gouge + 0.24 g Al2O3 + 0.69 g $Fe_2O_3^T$ + 1.12 g K_2O	30.37
High damage zone (4)	100 g wall rock – 15.32 g SiO_2 – 1.46 g Al_2O_3 – 0.02 g $Fe_2O_3^T$ – 5.80 g CaO – 1.91g Na_2O – 0.07 g MnO_2 – 3.22 g LOI – 0.08 g P_2O_5 → 72.78 g gouge + 0.19 g MgO + 0.48g K_2O	27.22
Low damage zone (4)	100 g wall rock – 10.07 g SiO_2 – 1.29 g Al_2O_3 – 0.02 g $Fe_2O_3^T$ – 4.15 g CaO – 1.36 g Na_2O – 0.04 g MnO_2 – 1.93 g LOI – 0.05 g P_2O_5 → 72.78 g gouge + 0.18 g MgO + 0.22 g K_2O	18.40

743
744
745

https://doi.org/10.5194/se-2020-117
Preprint. Discussion started: 28 July 2020

Solid Earth
Discussions
Open Access
EGU

746 **Figure 1**

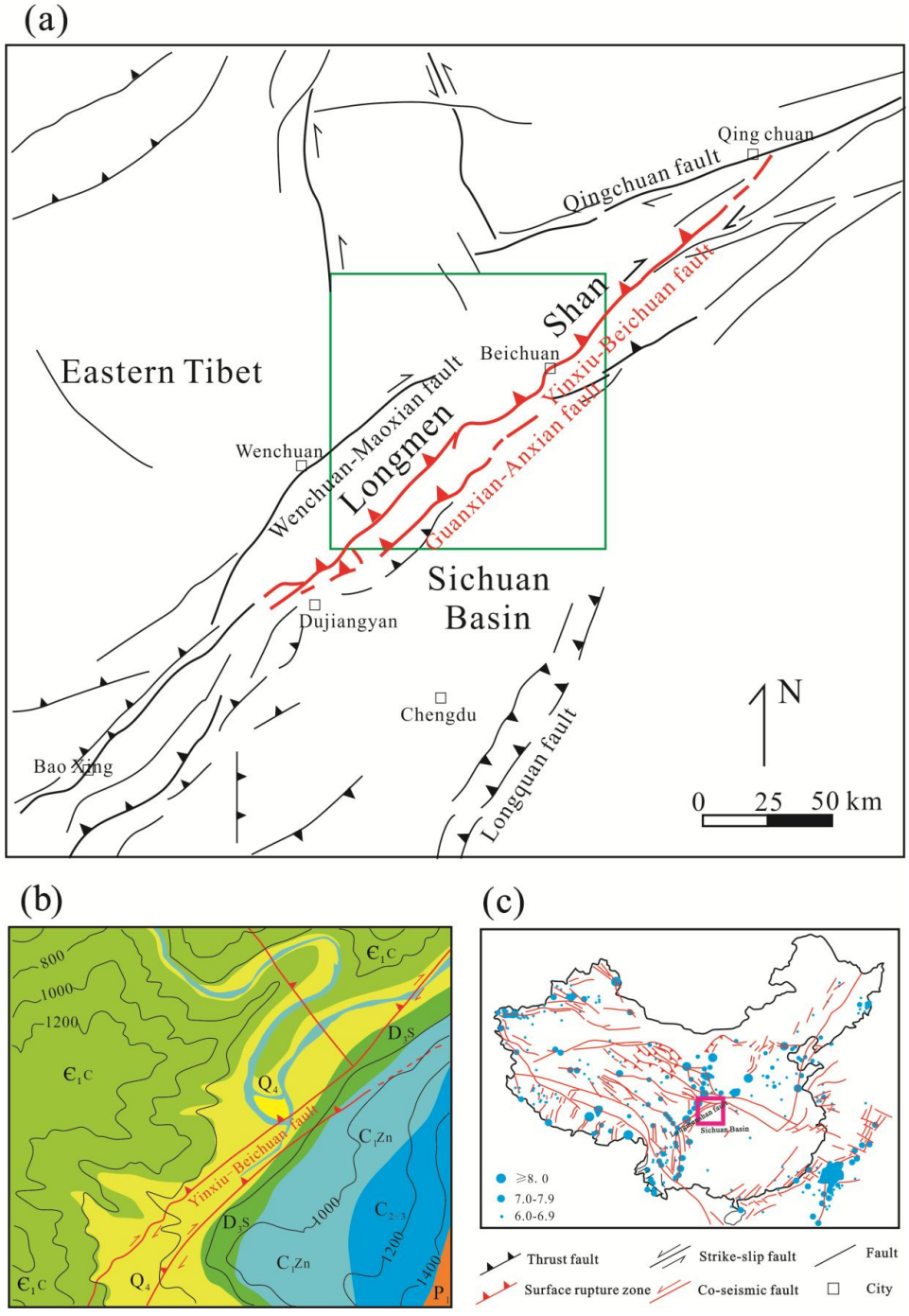

747

https://doi.org/10.5194/se-2020-117
Preprint. Discussion started: 28 July 2020

748 **Figure 2**

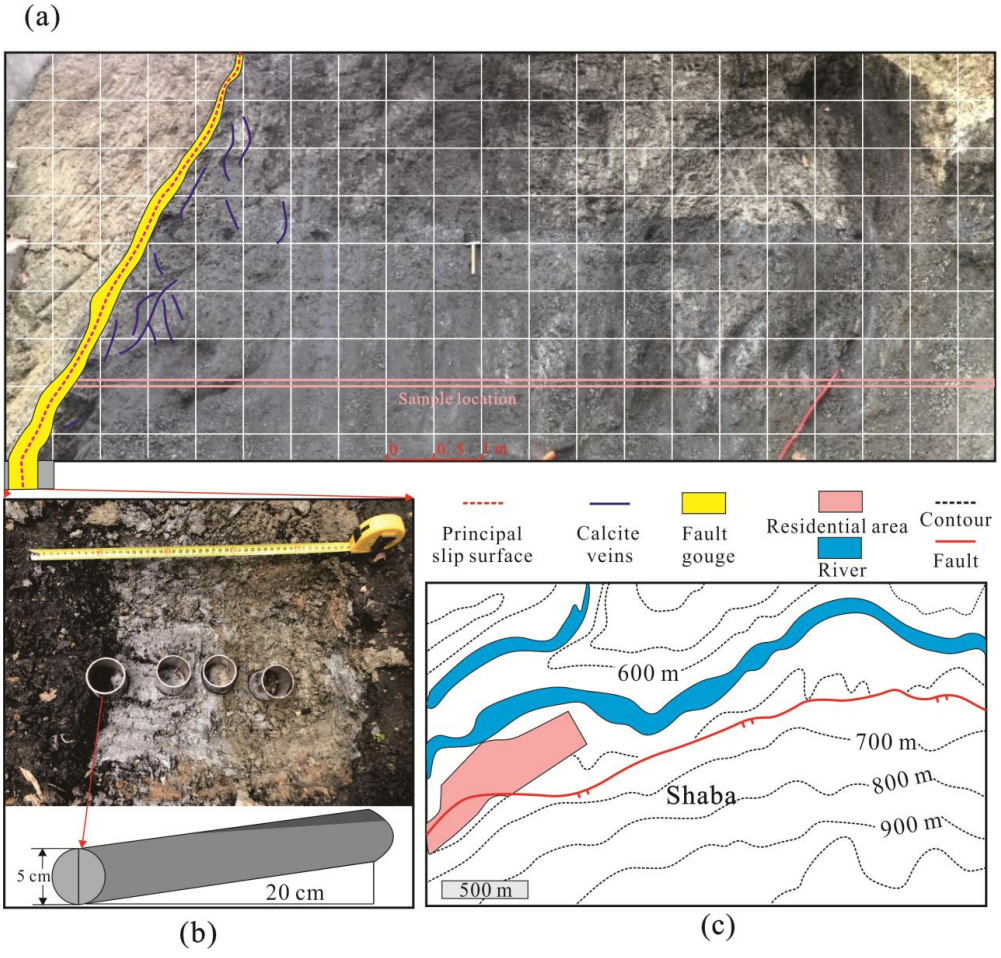

749

https://doi.org/10.5194/se-2020-117
Preprint. Discussion started: 28 July 2020

Solid Earth
Discussions
Open Access
EGU

750

Figure 3

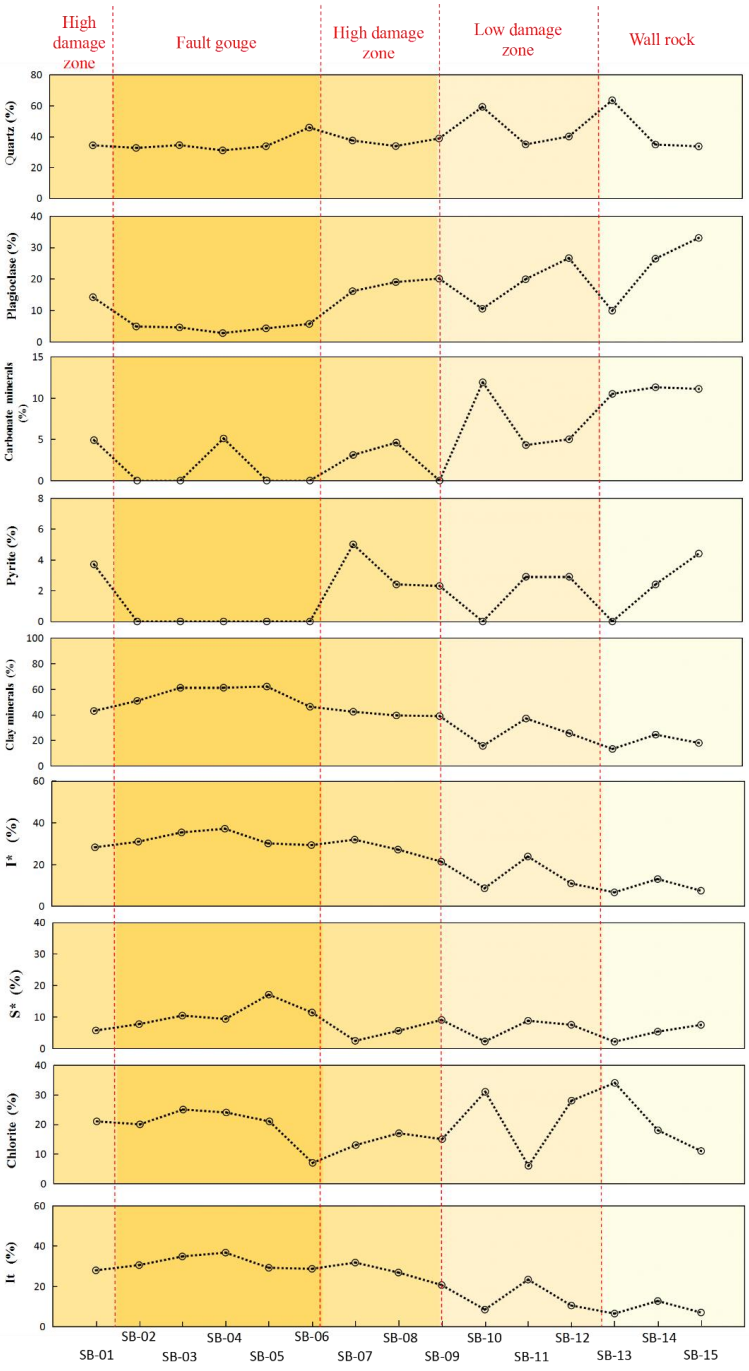

751

https://doi.org/10.5194/se-2020-117
Preprint. Discussion started: 28 July 2020

Solid Earth
Discussions
Open Access
EGU

752

Figure 4

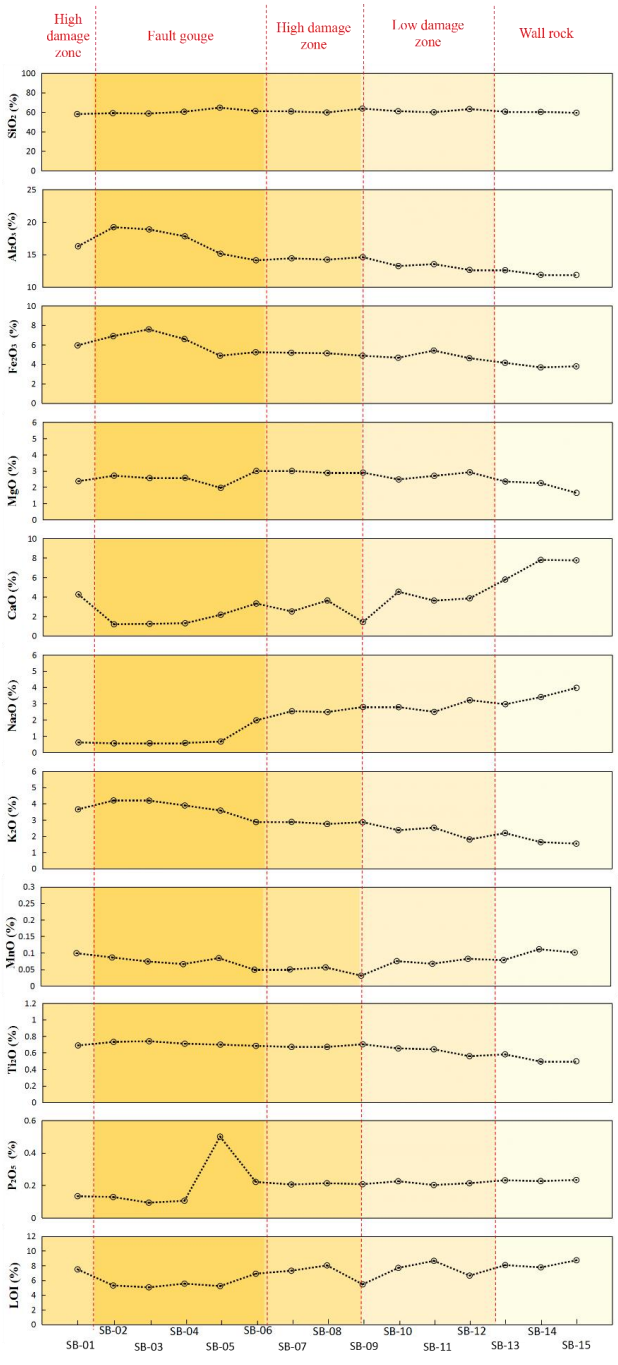

753

https://doi.org/10.5194/se-2020-117
Preprint. Discussion started: 28 July 2020

754

Figure 5

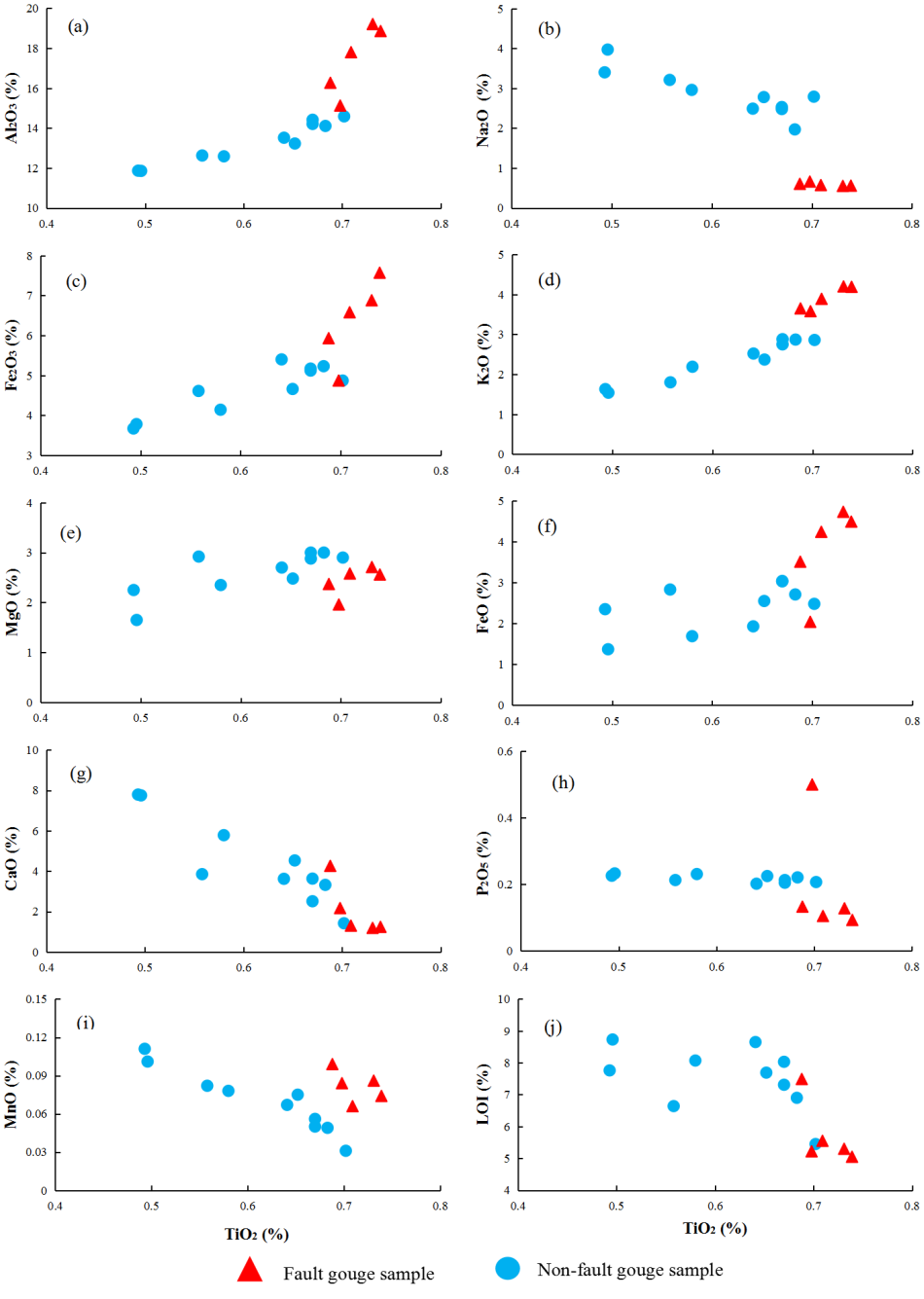

755

https://doi.org/10.5194/se-2020-117
Preprint. Discussion started: 28 July 2020

Figure 6

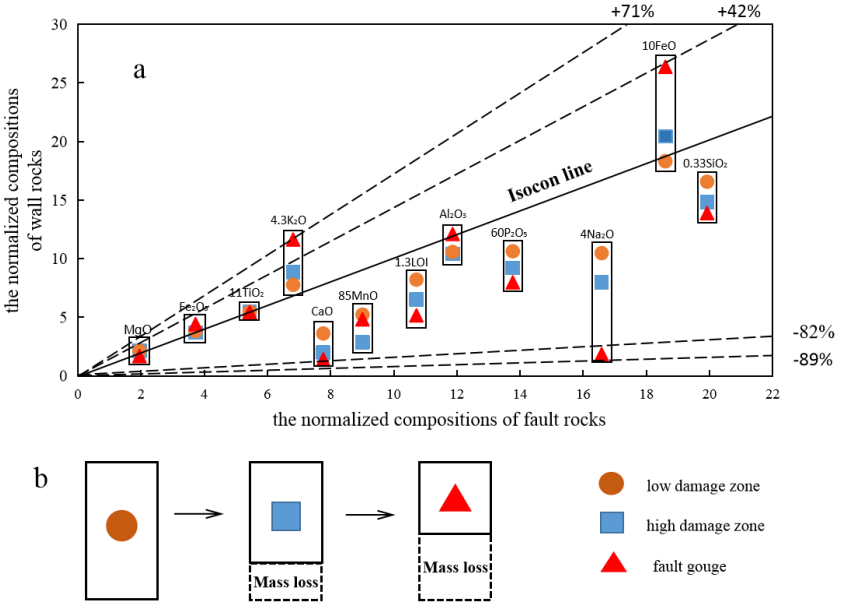

https://doi.org/10.5194/se-2020-117
Preprint. Discussion started: 28 July 2020

758 **Figure 7**

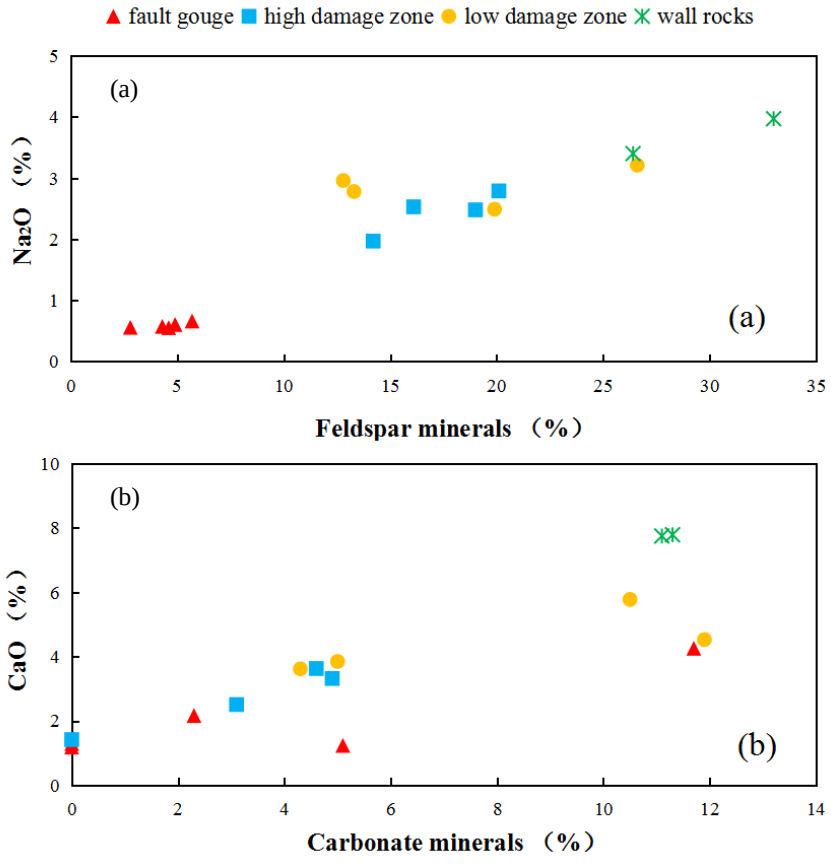

759

https://doi.org/10.5194/se-2020-117
Preprint. Discussion started: 28 July 2020

760 **Figure 8**

761 (a)

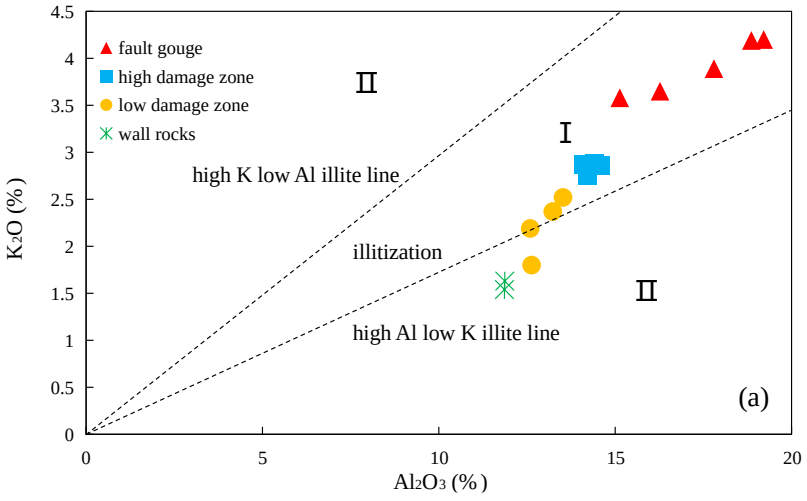

762

763 (b)

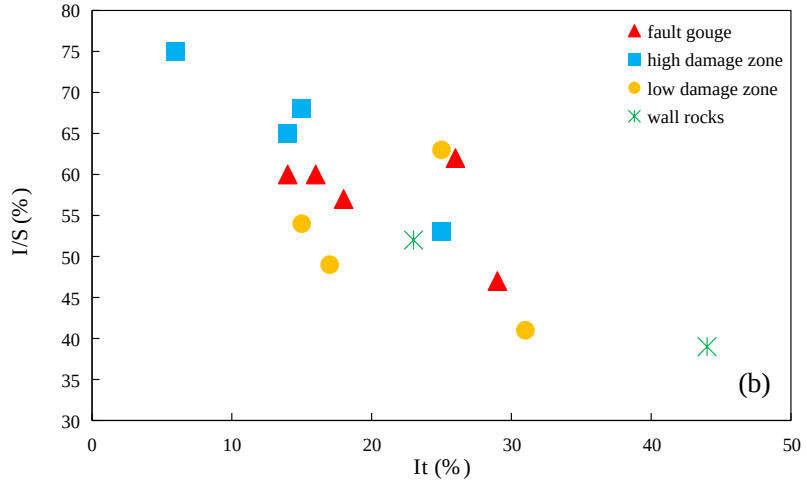

764

https://doi.org/10.5194/se-2020-117
Preprint. Discussion started: 28 July 2020

765 **Figure 9**

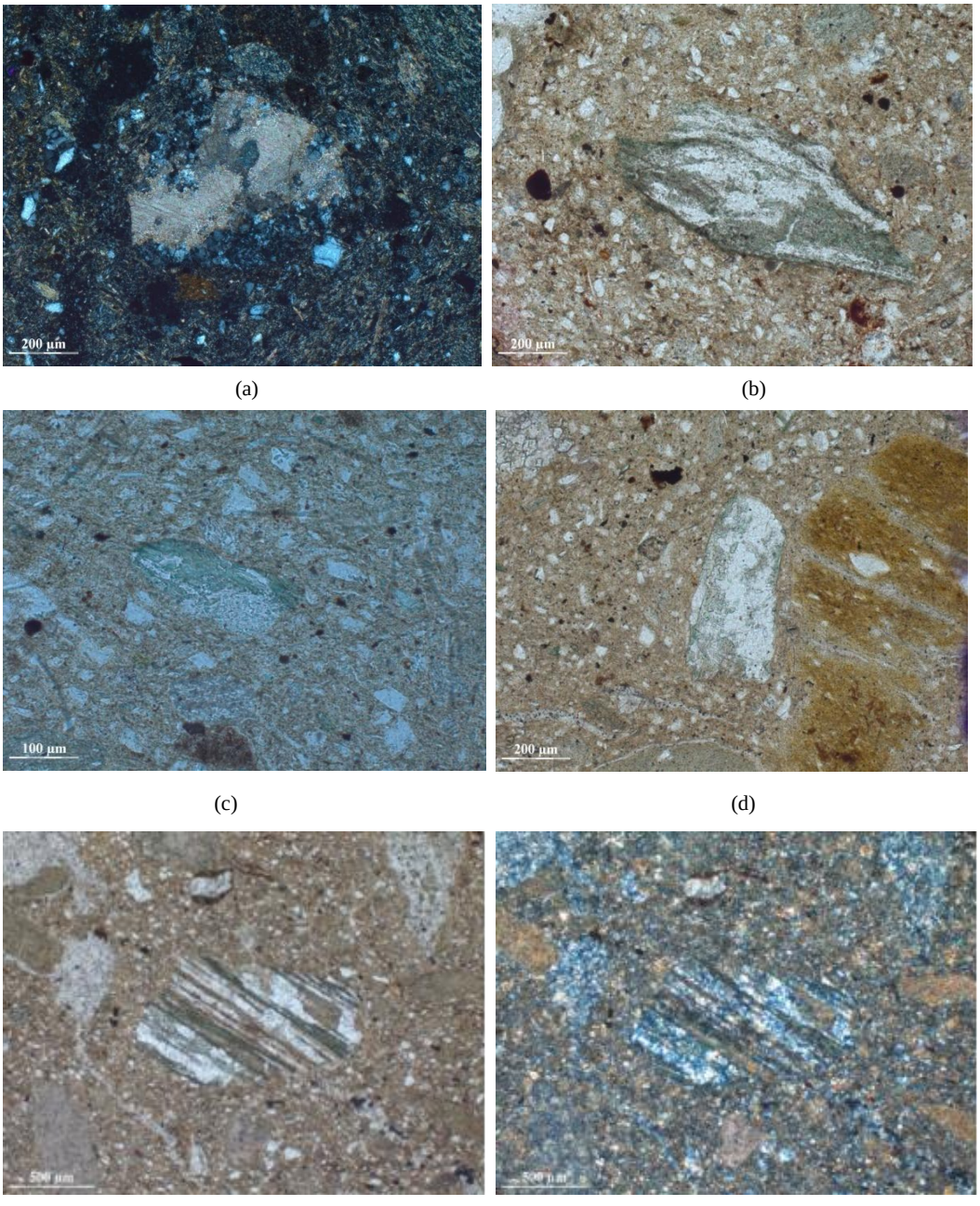

766
767 (a) (b)
768
769 (c) (d)
770
771 (e) (f)
772
773

https://doi.org/10.5194/se-2020-117
Preprint. Discussion started: 28 July 2020

774 **Figure 10**

775 (a)

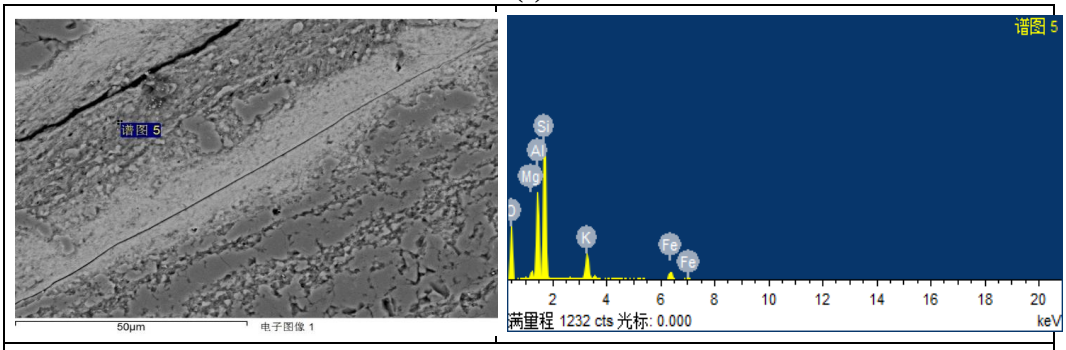

Element	Concentration (%)			Chemical component
	quality	atom	compound	
Mg	1.19	1.05	1.97	MgO
Al	13.40	10.68	25.31	Al_2O_3
Si	26.51	20.30	56.71	SiO_2
K	6.79	3.73	8.18	K_2O
Fe	6.08	2.34	7.83	FeO
O	46.03	61.89		
Total	100.00			

776

777 (b)

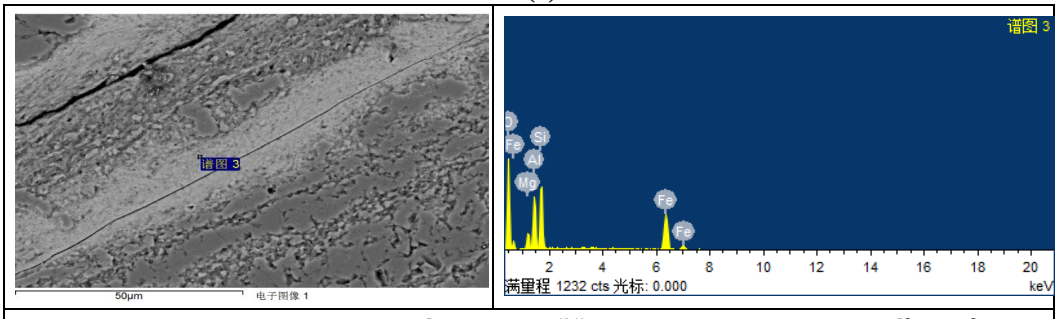

Element	Concentration (%)			Chemical component
	quality	atom	compound	
Mg	4.56	4.55	7.56	MgO
Al	11.21	10.09	21.18	Al2O3
Si	15.22	13.17	32.56	SiO2
Fe	30.08	13.08	38.70	FeO
O	38.93	59.11		
Total	100.00			

778

https://doi.org/10.5194/se-2020-117
Preprint. Discussion started: 28 July 2020

779 **Figure 11**

780

781

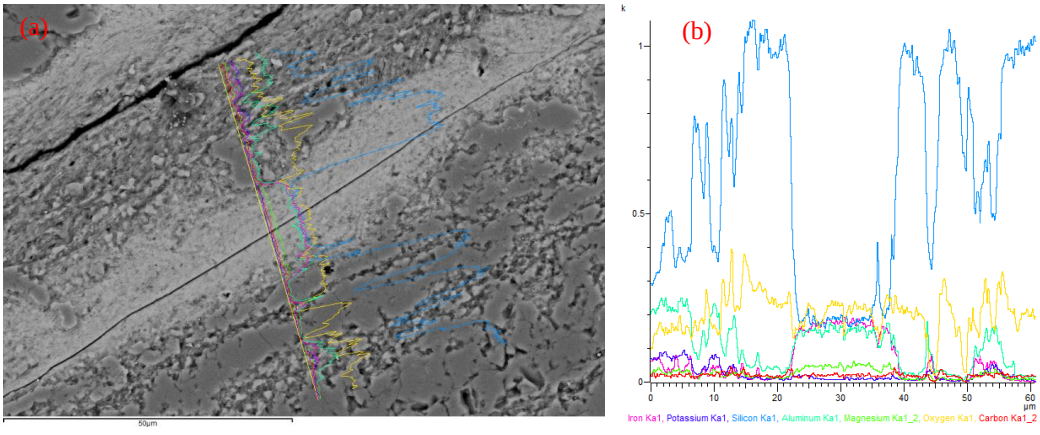

782

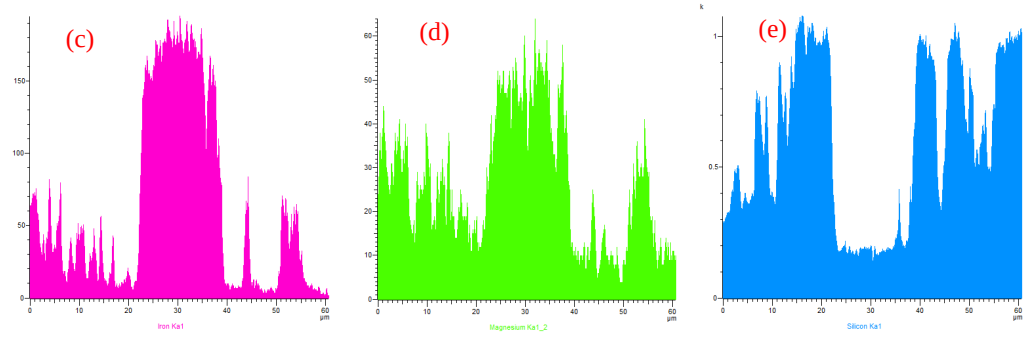

783

784

785

https://doi.org/10.5194/se-2020-117
Preprint. Discussion started: 28 July 2020

786 **Figure 12**

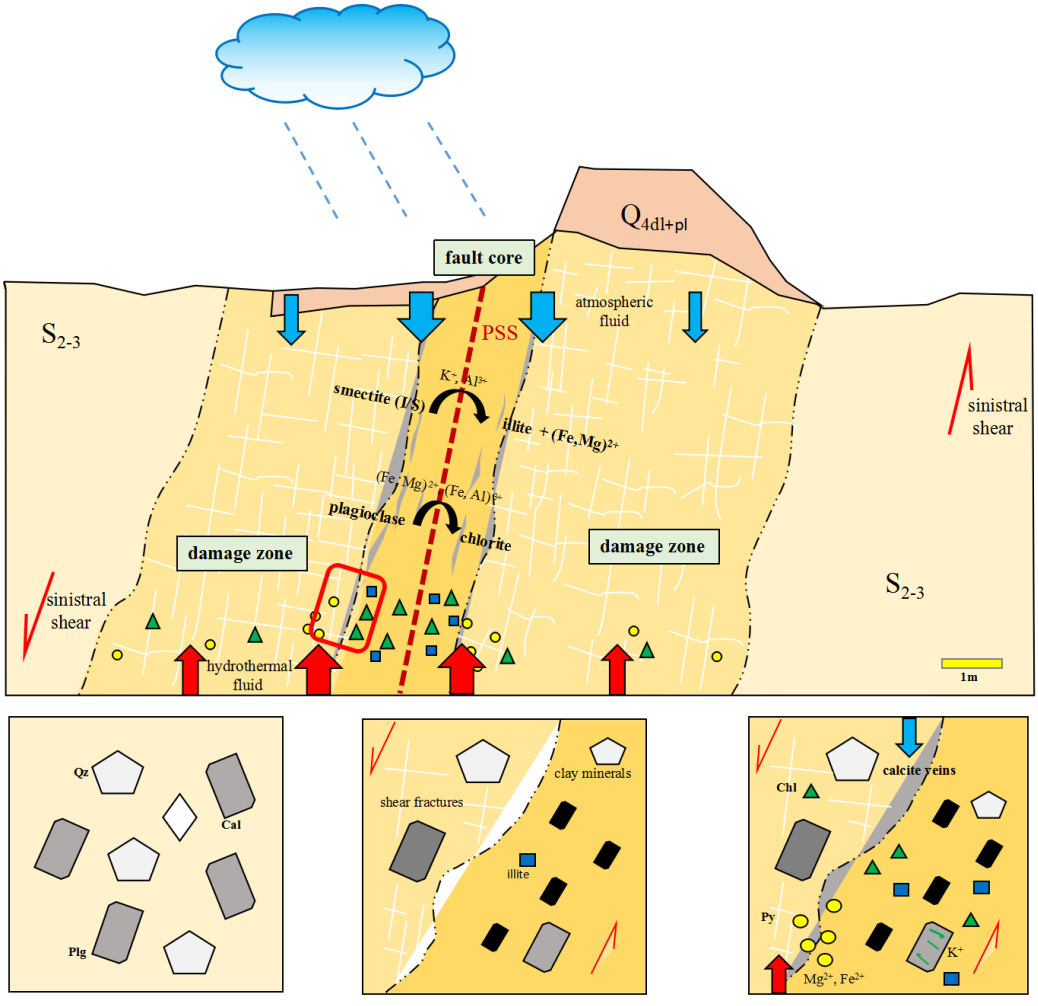

clastic sedimentary layer

The reduction in the grain size + decomposition of feldspar+ the formation and oriented arrangement of clay minerals

chloritization + precipitation of hydrothermal minerals + alteration of feldspar + the formation of calcite veins

787